13

Engineering and Technology

DESIGN AND DEVELOPMENT OF EASY-TO-ACCESS AUTOMATED COMPOSTING SYSTEM

Kreetha Somkeattikul[1*], Chaiyawoot Narintharangkul[2], Chinnathan Areeprasert[3], and Chaiyaporn Silawatchananai[4]

[1,2]Faculty of Engineering and Technology, Panyapiwat Institute of Management, Thailand
[3]Faculty of Engineering, Kasetsart University, Thailand
[4]Faculty of Technical Education, King's Mongkut University Technology of North Bangkok, Thailand
[*]**Corresponding author, E-mail:** kreethasom@pim.ac.th

Abstract

This article proposes the automated composter machine to treat the organic waste from the household or enterprise. The medium-size composter can convert the food waste to organic compost at the local site so that the volume of organic waste is reduced faster. In this work, the automation systems have been utilized in the composter prototype such as the programable logic controller (PLC) to deal with agitator, exhauster, and temperature control to optimize the treatment process period. Moreover, the graphical user interface (GUI) displaying with a 7-inched touchscreen is also introduced for monitoring, operating, and setting the composter machine, according to the raw material condition. Working with a touchscreen and GUI, the user can easily configure the required temperature and the operation of the agitator to mix the raw material with microorganisms from the cow dung. By maintaining the temperature in the chamber, the experimental result shows the performance of temperature control which the average error is less than 10% for several treatment processes. For various types of food waste, the performance of composting is evaluated by weighting which shows that 50-kg food waste can be composted to the fertilizer within 24 hours.

Keywords: Composting Reaction, Composting Chamber, Hot Composting, Automation systems

Introduction

Today solid waste is one of the biggest problems in the community. Around 50% of the waste is organic waste (Jayaprakash et al., 2018) such as leaves from the gardener, food waste from the household, cafeteria, and fresh market, which all can be converted into compost. The process of composting requires wet organic matter such as leaves, or food waste as known as green waste, and waiting to break down into humus for a certain period. It occurs by using microorganisms under specific conditions. Generally, there are two types of composting: anaerobic and aerobic composting. For anaerobic composting, there is no need to use oxygen to process, resulting in sludge, carbon dioxide, and methane. The treatment period is usually 20 – 40 days which is suitable for energy harvesting. While as aerobic composting uses oxygen for the process resulting in the composted matter, carbon dioxide, and water. The treatment period is usually 20 – 30 days so it is suitable for producing fertilizer (Tchobanoglous et al., 1993).

A programmable Logic Controller (PLC) is a programable device that is mostly used in industrial applications because of its durability and reliability. It can be programmed in several programming languages such as graphical language like Ladder Diagram (LD), Sequential Flow chart (SFC), and Function block diagram (FBD), or textual programming language like Instruction List (IL) and Structured Text (ST) (John & Tiegelkamp, 2001). Nowadays, not only turning ON/OFF but also

reading information sensor, implementing an advanced control algorithm can be archived by a simple PLC device such as the main controller for a robot manipulator (Bonfe et al. 2009), fault detection system (Işık et al., 2016) and Fuzzy based temperature controller (Wei 2017).

Research Objective

To introduce the alternative design of an automated composting system for supporting various types of food waste where the composite rate can be increased by applying a programable logic controller and environment control.

Literature Review

The design of the composter for the community considers the requirement of how to eliminate the ordure, accelerate the treatment process and result in the composed matter friendly to the environment. Thus, the composting reactor is usually designed to control the environment for composting such as temperature, and humidity by adding the air or stirring the matter to reduce the treatment time. Jayaprakash et al. (2018) proposed the design and development of compost bins based on the Quality Function Deployment (QFD) and Product Design Specification (PDS). For delivering design, the user's requirement is transformed into technical voices such as floor space area, less cost, ease of use, maintenance, lightweight, durable. In this work, the prototype of the composter has mainly three parts: compost-stater storage part, composting bin, and compost collection. It uses a rechargeable battery for mixing blades and calcium dioxide for heating. Even though this prototype has been validated in terms of product design, the processing time of the composter is not mentioned. Several works proposed the use of automation systems with the composter so that the user can operate and monitor, remotely. Elalami et al. (2019) proposed the smart composter controlled by several sensors such as NH3, PH, humidity, and temperature sensor to obtain the compost within 4 weeks. The actuator will be activated when the control variables are less than the setting conditions. Ahmadi et al. (2020) proposed a prototype reactor to compost agricultural wastes. This work applied a PI-controller to control temperature and humidity in different working conditions. The operator is also monitored and manipulated via a human-machine interface (HMI). Siti et al. (2020) proposed the rotary autonomous composter powered by solar cells. The consumption of energy has been addressed for component selection.

In Thailand, research on composting for a household has been proposed and conducted. Bumrungsalee (2011) proposed the design of a household composter with a 2-kg capacity. The proposed work used HDPE (High-density polyethylene) plastic dumb sized 40-cm diameter and 80 cm in height. Inside the dumb installed the pitch-blade agitator driven by the handwheel. The organic matter which has a combination of food waste and dried leaves with a weight ratio of 60:40 is mixed with microorganisms. After the treatment process for 24 days, the quality of composted matter was measured by the C/N ratio. Seeramai et al. (2014) proposed the product design approach-based garbage grinder for producing fertilizer. Nine experts in product design, mechanical design, and organic farming were assessed in terms of separation efficiency, grinding, and comfortable function. Soralump et al. (2019) proposed a small-size composter for municipal organic waste. This work shows compared the performance of compost bins with or without aeration. The average temperature during composting of two configurations is not different, but the average moisture content of the composter without aeration is greater than composter with aeration.

Methodology

1. Overall system design

1.1. Mechanical design

In this work, a composter was designed and constructed for the community with a capacity of 50-kg, as shown in Picture 1. It consists of a chamber, heating elements, agitator blades, and an exhaust fan. Composting chamber is made from stainless steel size 300 liters, diameter 800 mm. Two 2100-W heating elements are installed under the chamber in which heated matter was mixed with other sections by agitator blades. These removable agitator blades are attached to the shaft, which is laid along of the chamber. This part is driven by 1.5-HP single-phase AC motor and the 1:100 worm gear to reduce the speed at 15 rpm, approximately. A 4.5-inch diameter exhausting fan is attached at the front of the chamber with the carbon filter to vent the air out and eliminate the ordure. There is a lid on the top for put food waste into the chamber and another hatch for releasing the composted material.

Two thermocouple sensors are used to measure the temperature of composting materials and air inside the chamber.

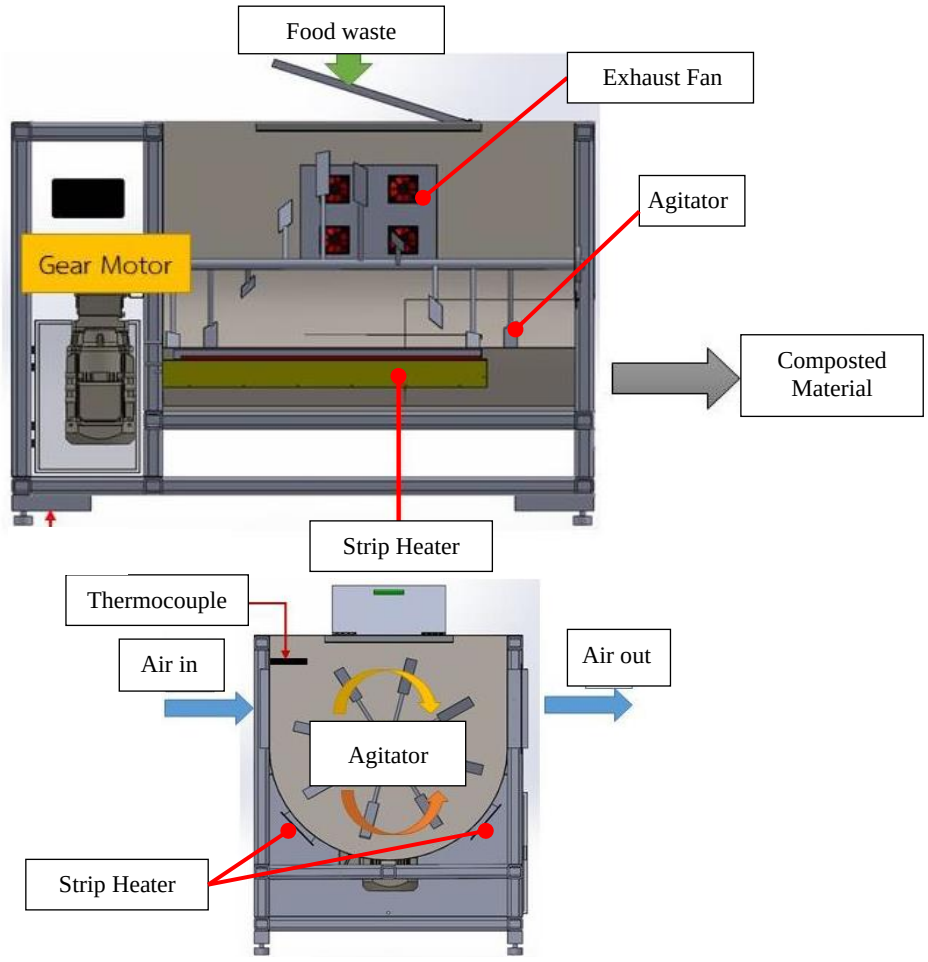

Picture 1: Components of composter

1.2. System architecture

This section describes the system architecture of the composter as shown in Picture 2, in which all components are controlled by PLC. In this work, PLC board FX1N-14MR is chosen as a

main controller which has eight inputs/six outputs for controlling all actuators, two analog inputs for reading the thermocouple sensors, and a serial communication port for interfacing with a 7-inch touchscreen. The user can set the configuration of compost condition, operate, and monitor the compost chamber through the touchscreen panel. There are two cabinet boxes containing the instrument components and high-power components, separately. As shown in Picture 3, the control box has PLC board, relay for fan control, solid-state relays for heater control, and 24-VDC switching power for providing the DC voltage to PLC, thermocouple transmitter, and touch screen panel. The power box has AC power terminal, motor terminal, and two magnetic contactors for motor direction control.

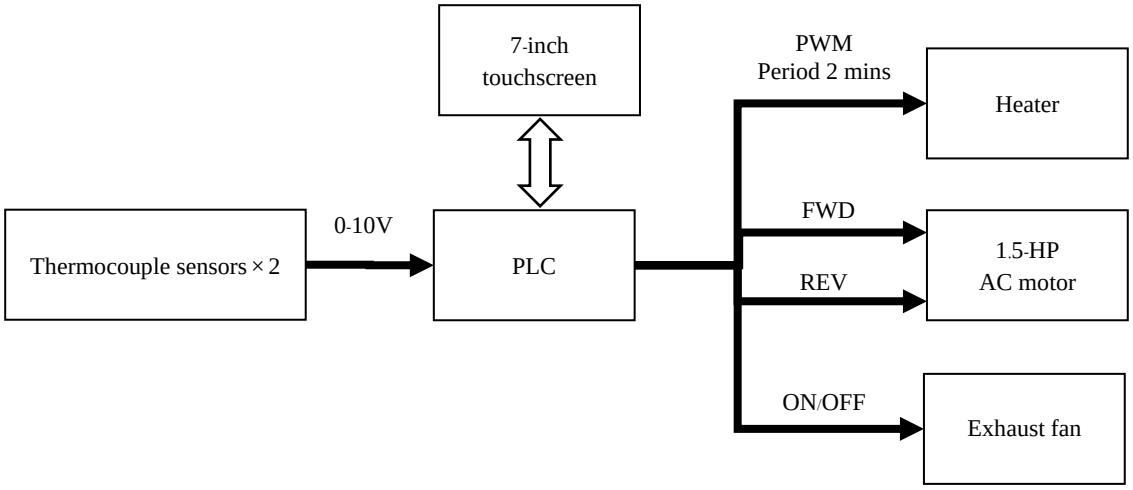

Picture 2: System architecture of composter

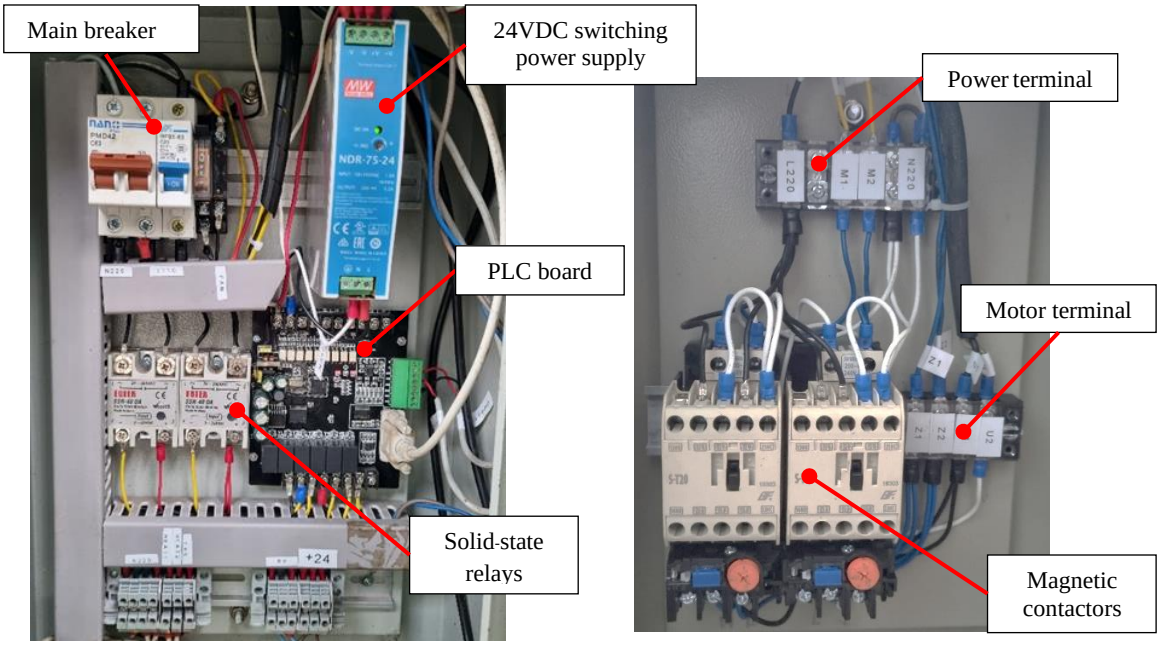

Picture 3: Components of composter

1.3. User interface and operation

The advantage of using a touchscreen panel over the traditional panel is that the users can monitor and operate the composter via a single device. Thus, it reduces the number of electrical parts applied so that it makes the system be compactness. Several screens can be included and switched by pressing the button on the side screen.

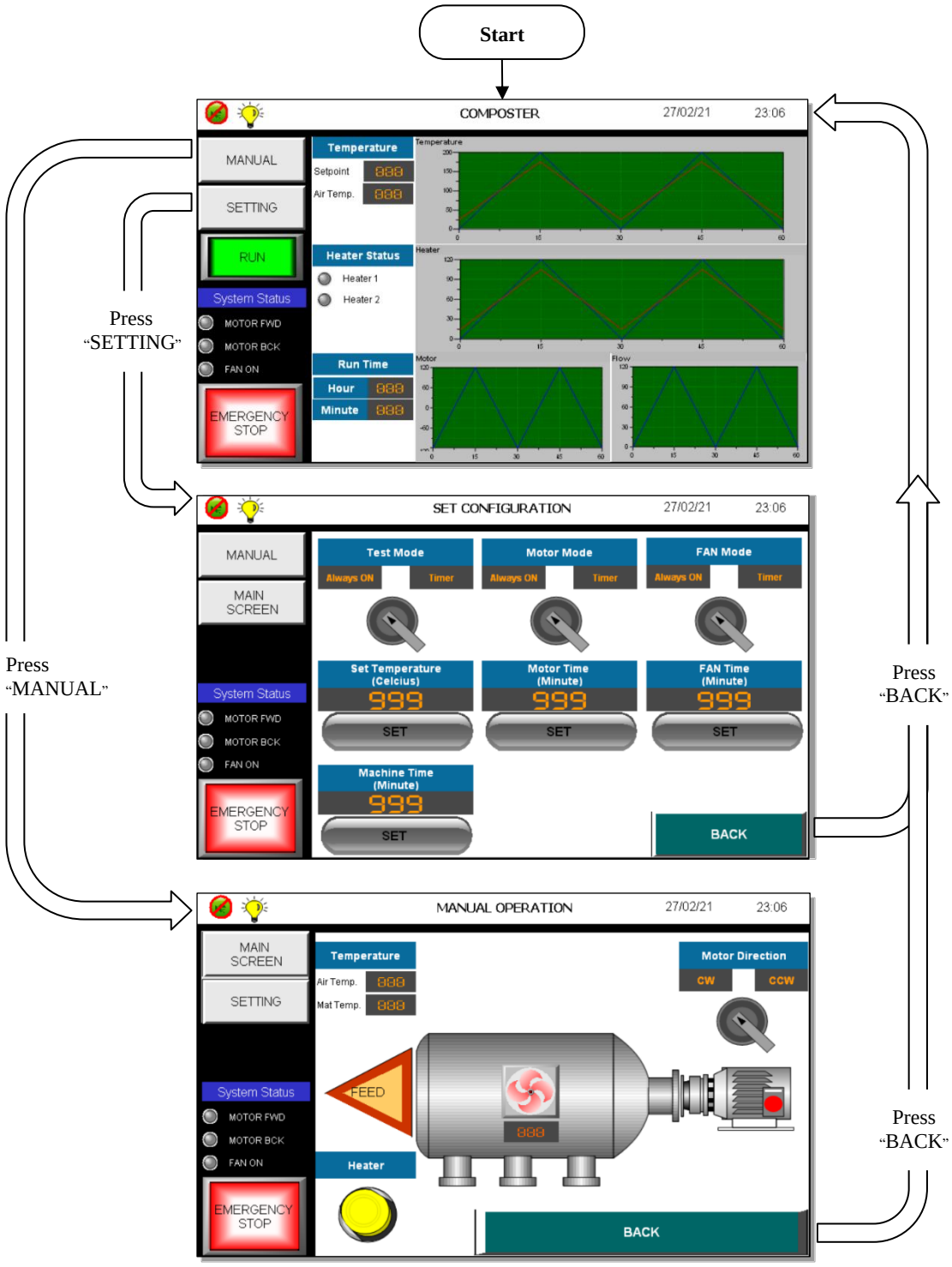

Picture 4: The user interface of the composter

Picture 4 shows the design of graphical user interface (GUI) screens and their flows. There are three main screens: MAIN, MANUAL, and SETTING which can be selected individually. In MANUAL mode, the user can turn ON/OFF each equipment manually for service purposes. In SETTING mode, the user can configure all parameters that are suitable for each food waste such as the setpoint value of temperature, the period time for turning ON/OFF agitator motor and exhausting fan, and the time for composting of each batch, Lastly, in RUNNING mode, all actuators are operated according to defined configuration. During composting process, the user can monitor all parameters such as measured temperature, state of agitator blade, and fan as time history plots.

2. Organic matter preparation

The raw material consists of food waste from either a fresh market or cafeteria, mixed with dried cow dung. Picture 5 represents the example of vegetable waste and dried cow dung that used for the experiment. To verify the performance of the composter, the organic matter was prepared at a capacity of 50 kg. Table 1 and Table 2 describe the weight ratio of raw material for each batch. Observably, the raw material batch No.2 has more moisture than batch No.1's.

Table 1: Weight ratio of raw material (Batch No.1)

No.	Type of organic matter	Weight (kg)
1	Vegetable waste	20
2	Dry cow dung	30

Table 2: Weight ratio of raw material (Batch No.2)

No.	Type of organic matter	Weight (kg)
1	Vegetable waste	18
2	Food waste	12
3	Dry cow dung	20

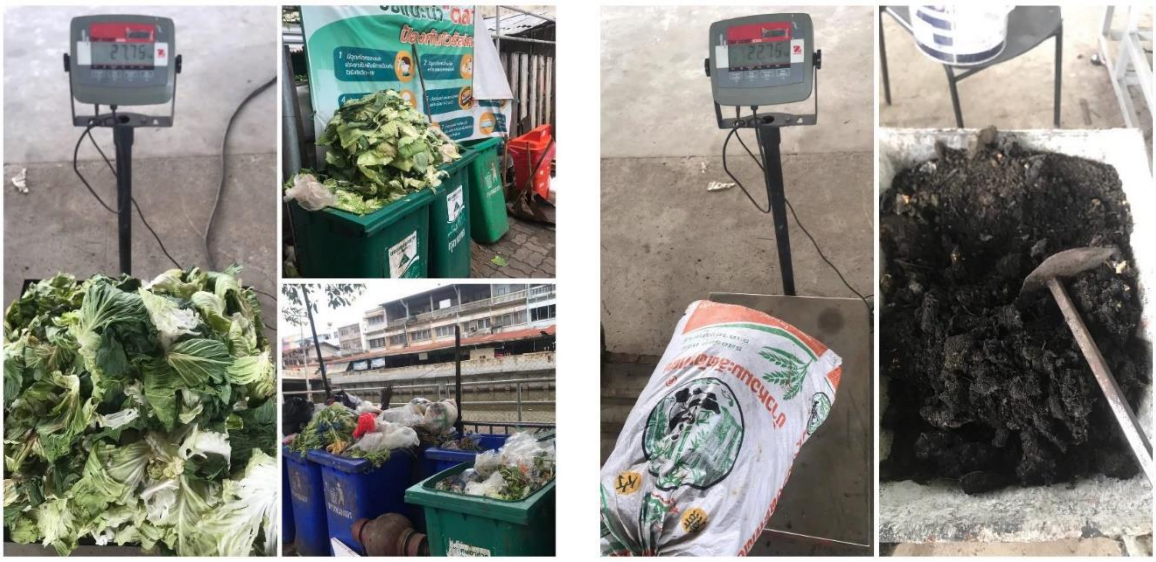

(a) Vegetable waste (b) Cow dung

Picture 5: Organic waste preparation

Results

This section compares the result of temperature control when the raw material of the composter has difference moisture and ratio. Sokač et al. (2022) proposed the mathematical modelling and statistical optimization techniques for enhancement of composting processes. The temperature is greater than 45 °C leading to another composting phase but must not exceed 65 °C. In this experiment, the setpoint value of is set at 50 °C. The system measuring temperature was recorded every hour. The working period of the composter is 24 hours. Picture 6 shows the time history of the temperature inside the chamber during the batch No.1 process. Initially, the temperature inside the chamber was at 34 °C and slightly was increased to the final value by heater elements after 6 hours.

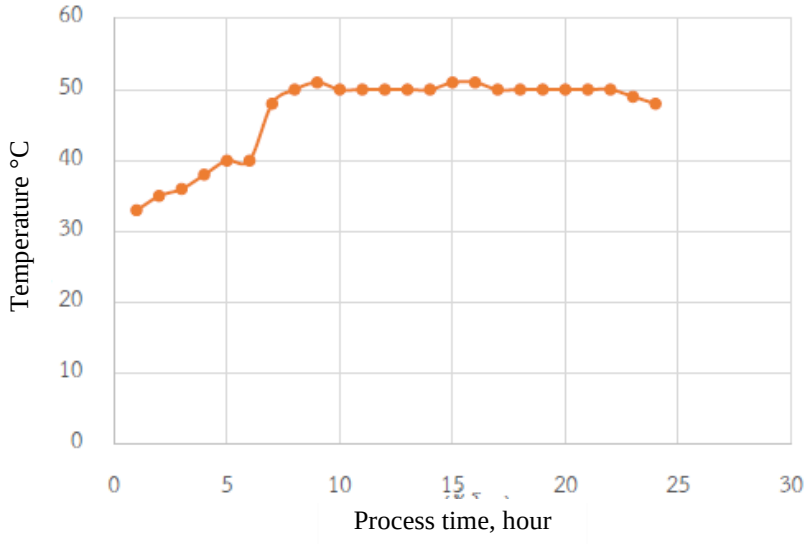

Picture 6: Temperature response of chamber during batch No.1

Picture 7 shows the time history of temperature in which the raw material Batch No.2 has more moisture. The result shows that there 25% overshoot of temperature in the chamber after 10 hours of composting. However, the steady-state value reached 50 °C after 17 hours of treatment.

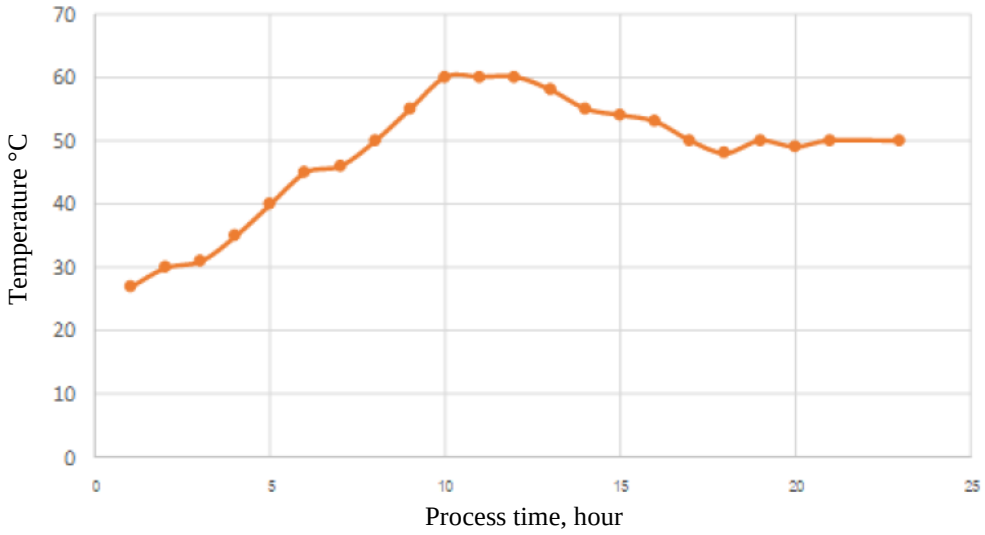

Picture 7: Temperature response of chamber during batch No.2

To test the operation of the composter for a long period, the treatment process period was set for 48 hours. In this experiment, the raw material has a ratio like batch No.2 and the setpoint temperature was set at 45 °C. Picture 8 shows the time history of the temperature inside the chamber that was recorded every hour.

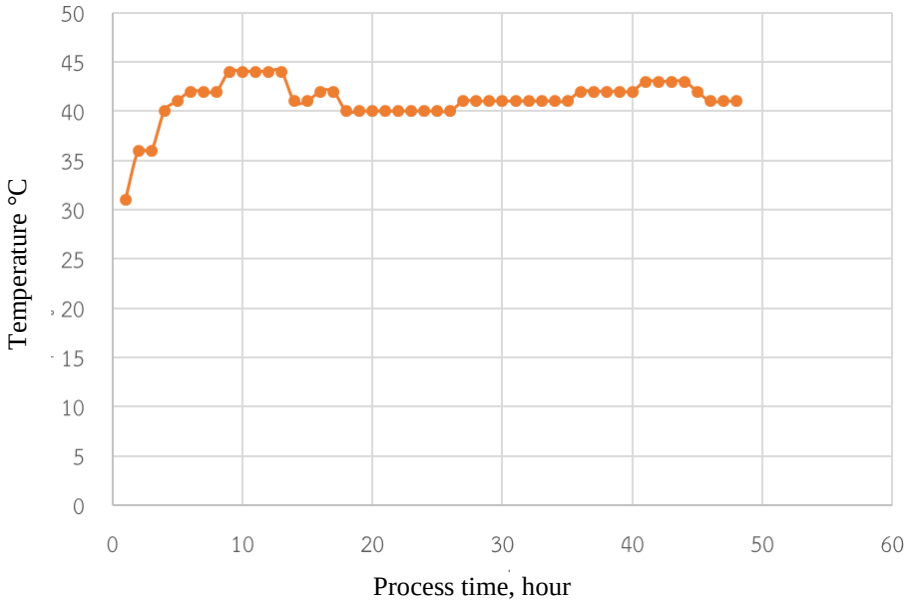

Picture 8: Temperature response of chamber for a long period experiment

For the appearance of composting material, both batches provide the dried black color material as shown in Picture 9. However, there is a small lump in the composted material.

(a) Batch No.1 (b) Batch No.2

Picture 9: Composted material after 24-hour treatment

Discussion

The performance of temperature control during composting is evaluated in the steady-state region. According to Picture 6, the average error between setpoint and actual temperature is 0.11 °C which the percentage error is 0.22%. For composting in batch No.2, the average error between setpoint and actual temperature is 0.19 °C which the percentage error is 0.38%. In Picture 8, the setpoint was set at 45 °C and the treatment period was set for 48 hours. The average error is 3.02 °C which the percentage error is 6.04%

The performance of 24-hours composting is compared and evaluated by weighting. The result in Table 3 shows that food waste in Batch No. 2 produces the composted material due to the loss of moisture. Table 4 compares the weight of composted material for the difference treatment period.

Table 3: Comparison of the composted material in weighting

Batch No.	Before treatment weight (kg)	After treatment weight (kg)	Weight loss (%)
1	50.0	46.0	8.0
2	50.0	44.0	12.0

Table 4: Comparison of the composted material in treatment period

Treatment time (hours)	Before treatment weight (kg)	After treatment weight (kg)	Weight loss (%)
24	50.0	46.0	8.0
48	50.7	37.15	26.73

During the 48-hour treatment process, several parts of the composter were observed that can be summarized below list:

1. The blade of the agitator can mix the raw material for 50.7 kg which is greater than the maximum capacity. The result shows that there is no crack or any damage in the mechanical part.

2. In the electrical system, the torque provided by the motor is required proportional to the volume of raw material. For the 48-hour treatment process, the motor-operated normally. However, their contamination such as bone or sticks in the food waste may lead to the problem. Thus, the raw material should be grinded or separated from this impurity before put in the chamber even though there overload relay to protect the exceeded current of the motor.

3. For temperature distribution, the amount of food waste has affected to distribution the temperature from the heat source to other sections. By using a bidirectional agitator, the overall temperature was slightly increased due to the moisture from food waste. Temperature control is applied to compensate until the reading temperature reaching to the setpoint value

Conclusion

In this work, the PLC-based composter has been proposed to convert the food waste be a composted material. Working with a touchscreen and GUI, the user can easily configure the required temperature and the operation of the agitator to mix the raw material with microorganisms from the cow dung. Comparing the traditional method, the machine applied temperature control and a bidirectional agitator so that the environment inside the chamber matched with the composting condition automatically. To verify the performance of composting, the raw material from the different sources was composted for 24-hour and 48-hour treatment processes. The result shows that the prototype of the composter can operate automatically for a long period of treatment and provide the composted matter that can used as fertilizer. For an environmental point of view, the volume of food waste is reduced by 8 – 12% within 24 hours and the ordure problem is eliminated by a carbon fiber filter. In summary, the automated composter is developed to reduce the amount of food waste and provide the natural fertilizer faster by control the composting condition.

Acknowledgment

We also want to express our sincere gratitude to the Department of Mechanical Engineering, Faculty of Engineering, Kasetsart University, and Dolphin Industries Co., Ltd. for supporting the working space and the raw materials.

References

Ahmadi, T., Casas Díaz, C.A., García Vera, Y.E., & Escobar Escobar, N. (2020). A prototype reactor to compost agricultural wastes of Fusagasuga Municipality. Colombia. *Agronomy Research. 18*(2), 314–323.

Bonfe, M., Vignali, M., & Fiorini, M. (2009), PLC-based control of a robot manipulator with closed kinematic chain. The *2009 IEEE International Conference on Robotics and Automation* (pp. 1262-1267). https://doi.org/10.1109/ROBOT.2009.5152281

Bumrungsalee, W. (2011). Household Composter. *The 21th Thai Institute of Chemical Engineering and Applied Chemistry Conference* (1 – 5), Prince of Songkla University. Hatyai, Songkhla.

Enoiu, EP. (2015). *Programming languages popularity and implications to testing programmable logic controllers*. PeerJ PrePrints. *9*(3), 2-4, https://doi.org/10.7287/peerj.preprints.879v1

Elalami, M., Baskoun, Y., Zahra Beraich, F., Arouch, M., Taouzari, M., & Qanadli, S. D. (2019). Design and Test of the Smart Composter Controlled by Sensors. *2019 7th International Renewable and Sustainable Energy Conference* (*IRSEC*), (pp. 1 – 6). https://doi.org/10.1109/IRSEC48032.2019.9078197

Jayaprakash, S., Lohit, H.S., & Abhilash, B.S. (2018). Design and Development of Compost Bin for Indian Kitchen. *International Journal Waste Resource, 8*(1): 323, http://doi.org/10.4172/2252-5211.1000323

John, D.K., & Tiegelkamp, D.M. (2001). *IEC 61131-3: Programming Industrial Automation Systems*. Berlin Heidelberg: Springer.

Işık, M. F., Haboğlu, M. R., Yanmaz, H., & Yilmaz, C. (2016). Fault detection and protection of induction motor by real time monitoring and controlling of the motor parameters. *Journal of Automation and Control Engineering*, 242-246. https://doi.org/10.18178/joace.4.3.242-246

Rangseesuriyachai, T., & Saricheewin K. (2018). Study of Organic Waste Composting with Aeration and Use of Crude Enzyme. *Journal of Engineering RMUTT, 16*(2), 1–12. https://ph01.tci-thaijo.org/index.php/jermutt/article/view/241943

Seeramai, K., Egwutvonda, S. & Saributr, U. (2014). Study and Design of grinders for producing fertilizer. *Art and Architecture Journal Naresuan University,* 5(2), 21–41.

Siti, F. Z., Elalami, M., Beraich, F. Z., Arouch, M., & Qanadli, S. D. (2021). Design and Production of an Autonomous Rotary Composter Powered by Photovoltaic Energy. *International Journal of Engineering Trends and Technology*, *68*(10), 1–10. https://doi.org/10.48550/ARXIV.2107.01993

Sokač, T., Valinger, D., Benković, M., Jurina, T., Gajdoš Kljusurić, J., Radojčić Redovniković, I., & Jurinjak Tušek, A. (2022). Application of optimization and modeling for the composting process enhancement. *Processes, 10*(2), 229. https://doi.org/10.3390/pr10020229

Soralump, C. (2019). Design of Small Household Composter for Municipal Organic Waste. *Kasetsart Engineering Journal*, *32*(108), 63-70.

Wei, F. (2017). The PLC-based Industrial Temperature Control System: Design and Implementation. *MATEC Web of Conferences*, 100, 303. https://doi.org/10.1051/matecconf/201710003031

OPTIMAL POST-CURING TIME OF DENTAL SG RESIN ON ITS MECHANICAL PROPERTIES

Natthawut Daoset[1], Nakarin Jullapram[2], Samroeng Inglam[3], and Nattapon Chantarapanich[4*]

[1,2,4]Faculty of Engineering at Sriracha, Kasetsart University, Thailand
[3]Faculty of Dentistry, Thammasat University, Thailand
[*]**Corresponding author, E-mail:** nattapon@eng.src.ku.ac.th

Abstract

This study aimed to investigate the effect of the post-curing process of dental commercial grade resin on mechanical properties under compressive load. The commercial-grade resin under consideration was Dental SG which was fabricated by Stereolithography (SL). Shape of test specimens was cuboid, their dimensions were 12.7 mm (length) x 12.7 mm (width) x 25.4 mm (height) according to ASTM D695-15. After SL fabrication, all samples were clean and dry before undergoing the post-curing process. The samples were divided into 4 groups, i.e. uncured group (no post-curing process), 1-hour post-curing, 2 hours post-curing, 3 hours post-curing, and 4 hours post-curing. All post-curing conditions were done at 50°C. The samples were tested by using a compressive process, performed according to ASTM D695-15. The crosshead speed was 1.3 mm/min, termination criteria were until the sample breakage. Mechanical properties including elastic modulus ultimate stress elongation at break yield stress and elongation at yield were extracted from the test. It revealed that the mechanical properties of the sample after post-curing were higher than an uncured sample. After 1 to 3 hours post-curing period, the samples were enhanced in all mechanical properties. At four hours post-curing period, elastic modulus and elongation at yield were dropped. This finding provides a recommendation to perform post-curing not to be over 3 hours. This is a benefit to a dental laboratory to optimize the processing time where dental devices using SL are manufactured.

Keywords: Stereolithography, Post-curing, Dental Device, Mechanical Properties

Introduction

Current design and manufacturing of various intra-oral dental tools have been digitalized, the obsoleting conventional method of making which may be inaccurate due to uncertainty of workmanship by a dental technician. One of the technologies which have increasingly gained importance in dental applications is Additive Manufacturing (AM). This process is done by adding material continuously layer-by-layer to build a 3D physical model. The AM technology provides personalized medical devices to be manufactured in a short time (Marchack, 2007). It relies on that this AM technique used for dental applications, especially the surgical guide, can improve accuracy in the treatment process (Giacomo et al., 2005). In addition, it can also reduce complexity in treatment (Zhang et al., 2021).

Stereolithography (SL) is one process important for medical applications because it provides good surface finishing, high accuracy, and high mechanical properties (Azari and Nikzad, 2009). In dental applications, devices manufactured by SL should have sufficient strength to provide stability of use during intra-operatives. (Unkovskiy et al., 2018). The mechanical properties enhancement of SL parts can be performed by post-curing processes such as using ultraviolet, high temperature, or gamma-ray. (Jindal et al., 2020; Chantarapanich et al., 2013; West et al., 2019). Since gamma-ray post-curing

processes are not cost-effective, difficult to perform, and involve hazardous radiation, therefore, recent studies on SL focused on SL fabrication parameters and non-irradiated post-curing processes. For example, (Jindal et al., 2020) focus on optimal post-curing temperature and time of Dental LT resin by using a suction cup, and (Chantapanich et al., 2013) studied the effect of printing parameter and UV post-curing period on Watershed 11122 resin.

Dental SG resin is one of the commercial currents and widely used for medical device fabrication (Unkovskiy et al.,2018; Whiley III et al.,2016; Salmi et al.,2020), and has been certified material for medical uses. Mechanical influence on Dental SG resin and post-cure 15 min with UV and store in light impermeable on 12 h and 48 h respectively (Unkovskiy et al., 2018). A current complication of SL medical device uses is the strength which some of them are broken during intra-operative. This may be from an improper post-curing process. In order to fulfill this related gap, this pilot study focused on finding the optimal post-curing condition of Dental SG based on different curing parameters. This would raise awareness of dental laboratories in the fabrication of medical devices related to dental applications.

Research Objective

The aim of this research was to investigate of influence of different UV post-curing times on mechanical properties of commercial dental graded resin Dental SG fabricated by SL technique.

Literature Review

AM is a fabrication technique to build a physical model without molding and or removing materials. This could reduce the amount of waste material including the cost of taking part. (Milovanovic et al., 2021; Chantarapanich et al., 2013; Whitley et al., 2016). SL process is one type of AM, which builds part by continuously laying material layer by layer. (Alharbi et al.,2015; Chantarapanich et al.,2013). SL can fabricate a physical model by migrating 3D Computer Aid Design (CAD) model in STL format to pre-processing software for G-code command preparation for controlling the SL machine (Väyrynen et al., 2016). Before part building, the SL machine may build support structure as necessary (Kalaskar & Schmidleithner, 2018; Chantarapanich, 2015) before each thin layer of resin was solidified by UV laser a, stacking up resin layer-by-layer (Chantarapanich, 2015; Touri et al., 2019). There are two building principles of SL i.e. conventional SL and up-side-down SL, as shown in Picture 1. For the conventional SL concept, the UV laser source is above the resin surface and the laser exposes directly to underneath resin on the platform (Han et al, 2008). The up-side-down SL concept is reversed of the conventional SL concept in which the UV laser source is below the resign. UV laser projects upward to the platform above it (Kalaskar & Schmidleithner, 2018). There are various dental use SL resins, for example, Dental SG resin (Unkovskiy, 2018; Rubayo, 2020), Dental LT clear resin (Jindal et al., 2020), high temp and black resin (Kreß et al., 2020). For dental SG resin was low cytotoxicity when compared to the example above (Kreß et al., 2020).

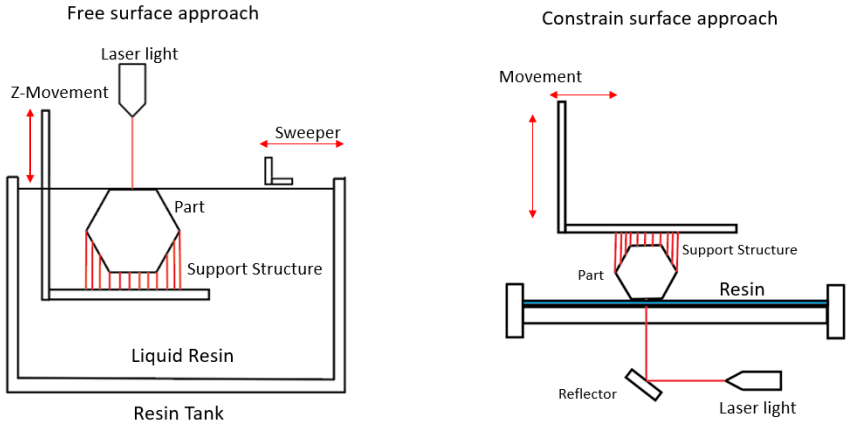

Picture 1: SL process (a) Conventional concept, (b) Up-side down SL concept

Typically, each type of SL resin requires certain process parameters, thermal curing temperature, and post-curing time that optimizes cost and part strength (Jindal et al., 2020; Kalaskar; Schmidleithner, 2018). SL in dental applications was suggested to build in 0 or 45 degrees orientation (Rubayo et al., 2021). In a previous study relating to the post-curing process, it has found that post-curing of PMMA over 60°C does not improve mechanical properties whereas a post-curing time of 10 minutes is sufficient for part strength (Reduko et al., 2021). Additional post-curing time does not improve mechanical properties. However, the work of (Chantarapanich et al.,2013) shows after 4 hours of the post-curing time of Watershed XC 11122 insignificantly improves mechanical properties. In addition, previous studies on Dental SG resin are relatively limited to a post-curing time of 15 min under UV radiation.

Methodology

Photopolymer epoxy resin

The photopolymer resin used in this current study is photo-cure Dental SG (Fromlabs Inc, USA) since it is commonly used in dental applications due to its biocompatibility (Formlabs, 2016). The liquid resin is stored in a supply tank made of plastic, the resin's appearance is yellowish transparency. The Dental SG is certified EN-ISO 10993-1:2009/AC:2010 (Biological evaluation of medical devices – Part 1 – Evaluation and testing), EN-ISO 7405: 2009/A1:2013 (Dentistry – Evaluation of biocompatibility of medical devices used in dentistry) and ISO 20795-1:2013 (Dentistry – Base Polymers – Part 1: Denture Base Polymers) (Formlabs, 2016). The mechanical properties data of Dental SG is provided in Table 1.

Table 6: Material properties of Dental SG

Description	Values
Flexural Strength	>= 50 MPa
Flexural Modulus	>= 1500 MPa
Hardness Shore D	>= 80
Charpy Impact Strength Unnotched	12 – 14 kJ/m^2

Source: (Formlabs, 2016)

Specimens, 3D printing device, 3D machine parameter

The specimen geometry for the compressive test was according to ASTM standard D695–15 (Standard test method for Compressive Properties of Rigid Plastics) (ASTM, Standard D695, 2015) which dimension of the specimen is 25.4 mm in height, 12.7 mm in width and 12.7 mm in length, as shown in Picture 2. Computer-Aided Software (CAD) (VISI, Hexagon AB, UK) was used to create a 3D digital model in STL format.

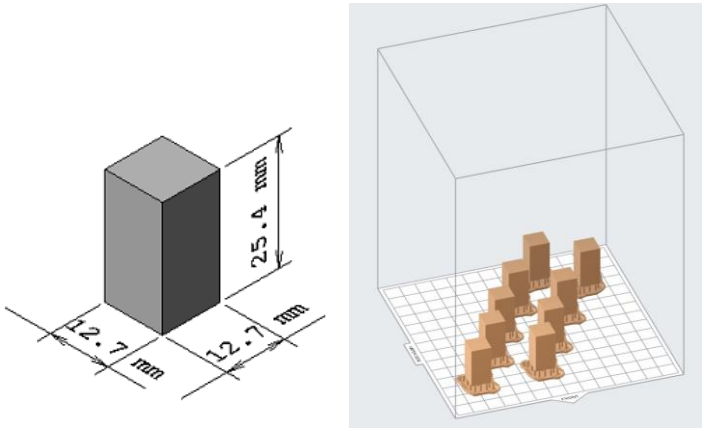

Picture 2: Specimen dimensions according to ASTM D695

PreForm (Fromlabs Inc, USA) was used for manipulating 3D CAD in preparing support structures and creating printing code (G-code) for SL machines. Specimens were fabricated in the vertical direction with a 0-degree orientation. Support structures were automatically generated using Preform (Fromlabs Inc, USA). Layer thickness for the part building is 0.1 mm. The 3D printer employed in this study is a Form 2 machine (Formlabs Inc, USA), its maximum printing volume is 145x145x175 mm. The SL 3D printer employed in this study operates based on the up-side-down concept. The machine received G-code from Preform (Fromlabs Inc, USA) via LAN. Prior to fabrication, it is needed to verify the resin remaining level from the supply tank. After that, the 3D printing automatically builds the physical part until complete. The fabrication process was in a dark room without an external light source to prevent unintended curing. The room is temperature-controlled at 26.4 +/-5 degrees and humidity at 55% RH +/-5 %.

Post-curing times experiment

After printing was finished, all specimens were cleaned with 70% Ethyl Alcohol to remove the excessive uncured resin. After that, the support structure was removed by using a flush cutter prior to undergoing the post-curing process. The curing was performed FromCure machine (Formlabs, Inc. USA). The specimens were separated into 5 groups, each group contained 3 samples. The specimens of each group were identified as an uncured group, 1-hr post-curing group, 2-hr post-curing group, 3-hr post-curing group, and 4-hr post-curing group respectively. For the post-curing group, the specimens were cured according to the group's designated time. The specimens were located in the post-curing chamber as shown in Picture 3.

Picture 3: Form cure machine and placement location

Compressive test

Universal Testing Machine UTM (UH-1000, Shimadzu Corp., Japan) was used to test the mechanical compressive properties of 3D printed specimens. The test protocol referred to ASTM standard D695–15 (Standard test method for Compressive Properties of Rigid Plastics) (ASTM, Standard D695, 2015). The specimen was loaded under a cross-head. The specimen was located at the center of the cross-head, as shown in Picture 4. The compressive test speed was constant at 1.3 mm/min. The termination of the test was until specimen damage. All datasets after the complete test were exported to CSV file format for mechanical properties analysis. The mechanical properties consider include elastic modulus, yield stress, ultimate stress, elongation at yield, and elongation at break respectively. All the mechanicals above by analyzed by using an in-house developed program.

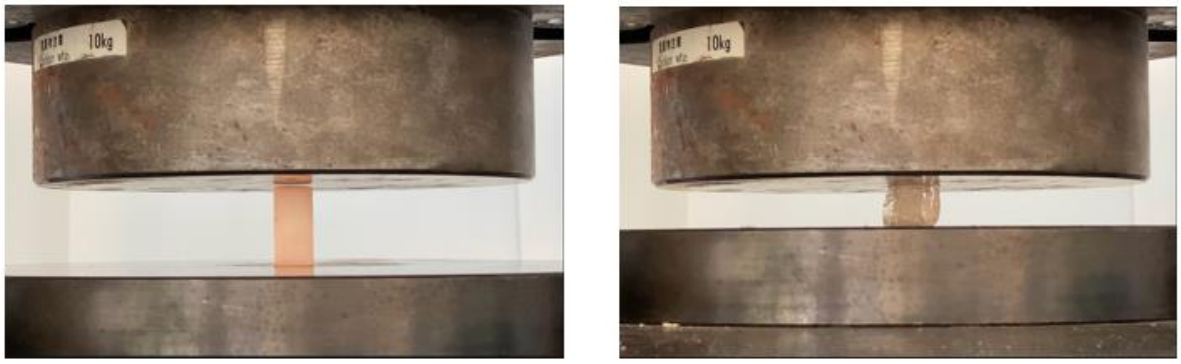

Picture 4: Specimen compressive before and after test

Results

All 3D printed specimens' dimensions were in good condition without incomplete geometry. After post-curing, the color of the sample was less transparent and more yellowish, as shown in Picture 5. Mechanical properties reported in each group were provided an average of 3 samples (n = 3), as shown in 2. The mechanical properties of post-cured samples were higher than uncured samples. After 1 to 3 hours post-curing period, the samples were enhanced in all mechanical properties. At four hours post-curing period, elastic modulus and elongation at yield were dropped. The average stress-strain curves of each group were shown in Picture 6.

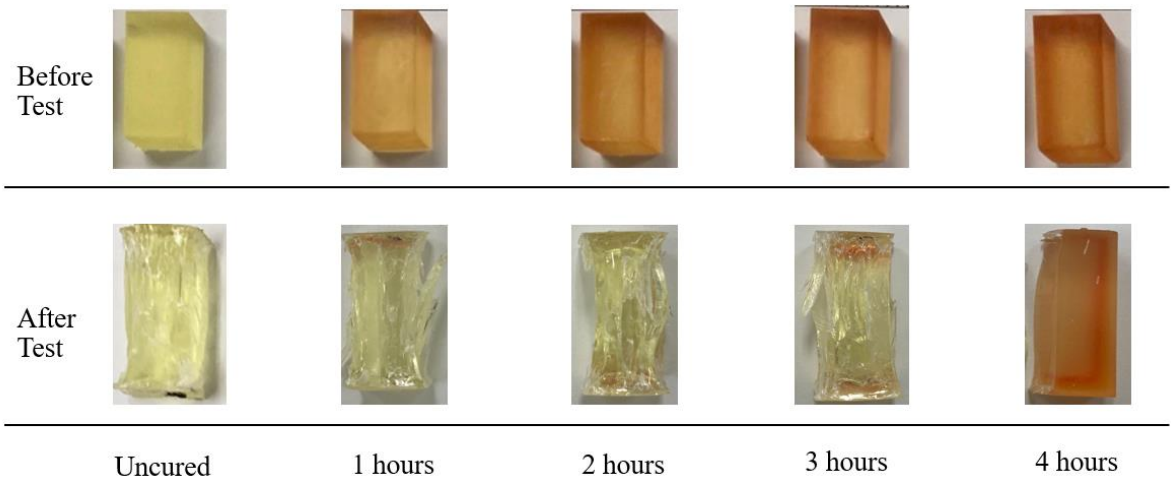

Picture 5: Specimen before and after compressive test

Table 2: Compressive mechanical properties

Description	Uncured	1 hours	2 hours	3 hours	4 hours
Elastic Modulus (MPa)	719.8 ± 32.0	1614.8±170.0	1656.5±16.6	1779.0±33.6	1603.4±11.5
Yield Stress (MPa)	21.61 ± 1.75	37.03±9.70	57.15±2.75	59.53±1.11	72.14±0.37
Elongation at Yield Stress	3.22 ± 0.36	2.59±0.91	3.65±0.19	3.54±0.07	4.28±0.48
Ultimate Stress (MPa)	240.3 ± 28.5	146.5±10.8	147.1±7.5	178.2±8.4	206.2±9.6
Elongation at Break	47.03 ± 1.43	34.68±0.89	32.63±0.77	35.13±0.91	36.99±0.58

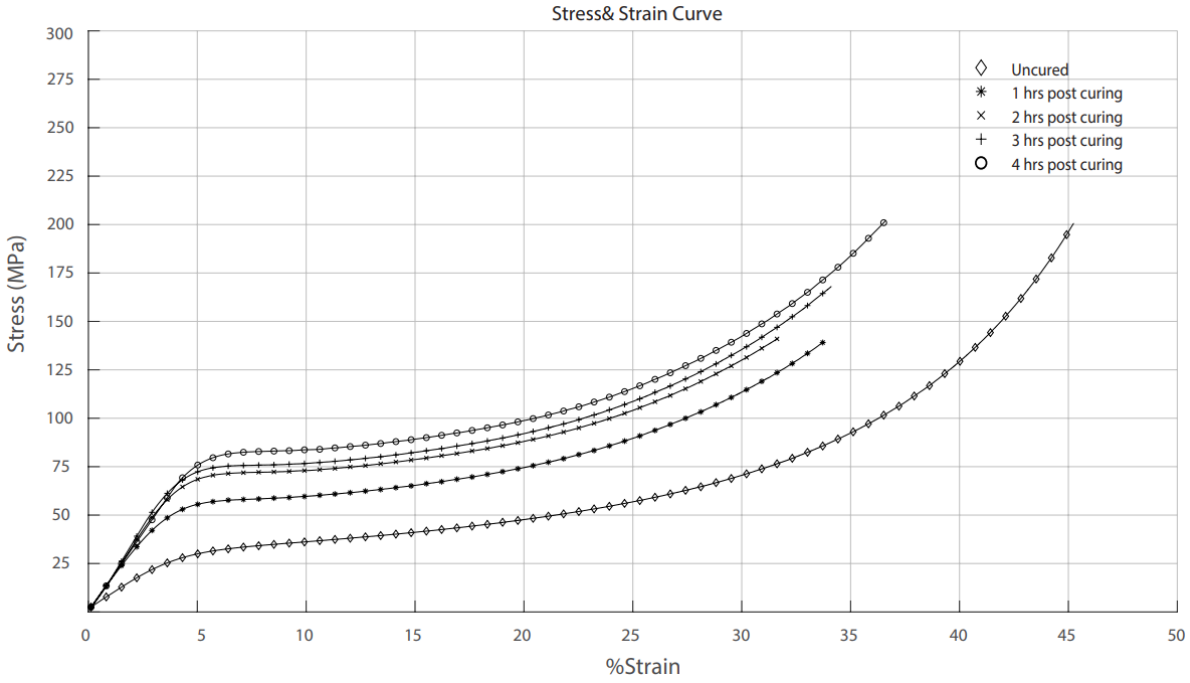

Picture 6: Stress & Strain average result compared to each post-cure process

Discussion

Additive manufacturing widely has been widely used for fabrication in dental applications, especially SL (Jockusch & Özcan, 2020). This is because SL is cost-effective, and produces accurate parts with low surface roughness. (Abarna et al., 2019; Alharbi et al., 2015; Chantarapanich, 2013). Dental SG resin is commercially available and widely used for medical device fabrication (Unkovskiy et al., 2018; Whiley et al., 2016; Salmi et al., 2020). However, the studies on mechanical properties after post-curing is limited. This study aimed to find the optimal post-curing time for commercial Dental SG resin that produces sufficient mechanical strength.

The mechanical properties reported in Table 2, i.e. elastic modulus and yield stress increase linearly in their values after post-curing and reach their maximum at 3 hrs. This can be explained that the longer time of UV exposure, it activates more chemical reactions via the photoinitiator contained in the sample, inducing a crosslink of monomer which produces polymer inside the sample (Bayarsaikhan et al., 2021; Santos et al., 2014).

After 3 hours of post-curing, mechanical properties were slightly dropped. Relation between elastic modulus-post-curing time, and yield-post-curing time between 1-3 hours are linear (Elastic Modulus (MPa) = Post-curing time (Unit: Hour)*321.94 + 637.66), Yield Stress (Unit: MPa) = Post-curing time (Unit: Hour)*12.36 + 12.42) which R-square values of 0.73 and 0.95.

In addition, the Dental SG became more brittle after post-curing. The result from this study may not directly comparable to the previous studies (Chantarapanich et al., 2013; Reduko et al., 2021), that was conducted on tensile load. However, the optimal post-curing time reported by (Chantarapanich et al., 2013; Reduko et al., 2021) is different approximately 2 hours and 50 minutes. According to this pilot study, the optimal post-curing time for Dental SG is 3 hours which is also different from other materials (Chantarapanich et al., 2013; Reduko et al., 2021). Thus, it is suspected that each resin may have a different optimal post-curing time for enhancing mechanical properties.

Conclusion

This study presents the investigation of mechanical properties of Dental SG resin under compressive load affected by different post-curing times. Based on the experimental results, mechanical properties are greatest after 3 hours of post-curing whereas some of the mechanical properties such as elastic modulus and yield stress were dropped after 3 hours of post-curing. Relations between elastic modulus-post-curing time and yield-post-curing time are linear.

References

Azari, A., & Nikzad, S. (2009). The evolution of rapid prototyping in dentistry: a review. *Rapid Prototyping Journal*, 15(3), pp. 216-225.

Abarna, J., & Maragathavalli, G. (2019). The evolution of rapid prototyping in dentistry- a review. *Journal of Pharmaceutical Sciences and Research*, 11(5), 1670-1675.

Alharbi, N., Osman, R., & Wismeijer, D. (2016). Effects of build direction on the mechanical properties of 3D-printed complete coverage interim dental restorations. *The Journal of prosthetic dentistry, 115(6),* 760–767.

ASTM, Standard D695 (2015). *Annual Book of ASTM Standards*. West Conshohocken: PA.

Bayarsaikhan, E., Lim, J.-H., Shin, S.-H., Park, K.-H., Park, Y.-B., Lee, J.-H., & Kim, J.-E. (2021). Effects of Postcuring Temperature on the Mechanical Properties and Biocompatibility of Three-Dimensional Printed Dental Resin Material. *Polymers, 13*(8), 1180.

Chantarapanich, N. (2015). Part Fabrication with Stereolithography Process. *The Journal of Industrial Technology 2015*, 1 January – April 2015. Thailand: College of Industrial Technology (CIT).

Chantarapanich, N., Puttawibul, P., Sitthiseripratip, K., Sucharitpwatskul, S., & Chantaweroad, S. (2012). Study of the mechanical properties of photo-cured epoxy resin fabricated by stereolithography process. *Songklanakarin journal of science and technology 2013*, Jan – Feb 2013. Thanland: Prince of Songkla University.

Di Giacomo, G. A., Cury, P. R., de Araujo, N. S., Sendyk, W. R., & Sendyk, C. L. (2005). Clinical application of stereolithographic surgical guides for implant placement: preliminary results. *Journal of periodontology, 76*(4), 503–507.

Dos Santos, R. L., de Sampaio, G. A., de Carvalho, F. G., Pithon, M. M., Guênes, G. M., & Alves, P. M. (2014). Influence of degree of conversion on the biocompatibility of different composites in vivo. *The journal of adhesive dentistry, 16*(1), 15–20.

Formlabs. (2016). Dental SG: Biocompatible photopolymer resin for form 2. Retrieved Oct 21, 2021, from https://formlabs-media.formlabs.com/datasheets/DentalSG-DataSheet.pdf

Han, L., Mapili, G., Chen, S., & Roy, K. (2008). Projection Microfabrication of Three-Dimensional Scaffolds for Tissue Engineering. *Journal of Manufacturing Science and Engineering, 130*(2), 021005-3.

Jindal, P., Juneja, M., Bajaj, D., Siena, F.L., & Breedon, P. (2020). Effects of post-curing conditions on mechanical properties of 3D printed clear dental aligners. *Rapid Prototyping Journal, 26*(8), 1337-1344.

Jockusch, J., & Özcan, M. (2020). Additive manufacturing of dental polymers: An overview on processes, materials and applications. *Dental materials journal, 39*(3), 345–354.

Schmidleithner, C., & Kalaskar, D. M. (2018). *Stereolithography*. United Kingdom: IntechOpen.

Kreß, S., Schaller-Ammann, R., Feiel, J., Priedl, J., Kasper, C., & Egger, D. (2020). 3D Printing of Cell Culture Devices: Assessment and Prevention of the Cytotoxicity of Photopolymers for Stereolithography. *Materials (Basel, Switzerland), 13*(13), 3011.

Marchack C. B. (2007). CAD/CAM-guided implant surgery and fabrication of an immediately loaded prosthesis for a partially edentulous patient. *The Journal of prosthetic dentistry*, *97*(6), 389–394

Milovanovic, A., Sedmak, A., Golubovic, Z., Mihajlovic´, K, Z., Zurki´c, A., Trajkovic´, I &. Milo˘sevi´c. (2021). The effect of time on mechanical properties of biocompatible photopolymer resins used for fabrication of clear dental aligners. *Journal of the Mechanical Behavior of Biomedical Materials*, *119*(1), 104494.

Rubayo, D. D., Phasuk, K., Vickery, J. M., Morton, D., & Lin, W. S. (2021). Influences of build angle on the accuracy, printing time, and material consumption of additively manufactured surgical templates. *The Journal of prosthetic dentistry*, *126*(5), 658–663.

Salmi, M., Akmal, J. S., Pei, E., Wolff, J., Jaribion, A., & Khajavi, S. H. (2020). 3D Printing in COVID-19: Productivity Estimation of the Most Promising Open Source Solutions in Emergency Situations. *Applied Sciences*, *10*(11), 4004.

Touri, M., Kabirian, F., Saadati, M., Ramakrishna, S., & Mozafari, M. (2019). Additive Manufacturing of Biomaterials − The Evolution of Rapid Prototyping. *Advanced Engineering Materials*, *21*.

Unkovskiy, A., Hai-Binh Bui, P., Schille, C., Geis-Gerstirfer, J., Huettig, F. & Spintzyk, S. (2018). Objects build orientation, positioning, and curing influence dimensional accuracy and flexural properties of stereolithographically printed resin. *Dental Materials*, *34*(12), 324-333.

Väyrynen, V. O., Tanner, J., & Vallittu, P. K. (2016). The anisotropicity of the flexural properties of an occlusal device material processed by stereolithography. *The Journal of prosthetic dentistry*, *116*(5), 811–817.

Whitley, D., 3rd, Eidson, R. S., Rudek, I., & Bencharit, S. (2017). In-office fabrication of dental implant surgical guides using desktop stereolithographic printing and implant treatment planning software: A clinical report. *The Journal of prosthetic dentistry*, *118*(3), 256–263

West, C., McTaggart, R., Letcher, T., Raynie, D., & Roy, R. (2019). Effects of gamma irradiation upon the mechanical and chemical properties of 3D-printed samples of polylactic acid. *Journal of Manufacturing Science and Engineering*, *141*(4), 41002

Zhang, J., Yang, Y., Han, X., Lan, T., Bi, F., Qiao, X., & Guo, W. (2021). The application of a new clear removable appliance with an occlusal splint in early anterior crossbite. *BMC oral health*, *21*(1), 36.

基于 ResNet50 网络模型融合 Mixup 算法的社区划分研究
COMMUNITY DIVISION BASED ON RESNET50 NETWORK MODEL AND MIXUP ALGORITHM

王海峰 [1]，李奇 [2]，董俊甫 [3*]，张德银 [4]，马轶哲 [5]
Haifeng Wang[1], Qi Li[2], Junfu Dong[3*], Deyin Zhang[4], Yizhe Ma[5]

[1, 2, 3, 4, 5] 中国南京工业大学浦江学院
[1, 2, 3, 4, 5]Nanjing Tech University Pujiang Institute, China
[*]**Corresponding author, E-mail:** 2446201357@qq.com

摘要

随着季节的更替，公共卫生问题频发，传染病的产生与蔓延对于公共卫生安全已经产生了较严峻的影响。一旦管控不及时，社区作为城市功能模块中最长久固定的人口聚集区必将首当其冲。究其原因，主要是社区在治理方面存在信息混乱，区域划分不明确等问题。因此合理有效地划分能使社区在面对突发卫生问题时更高效、有条理的进行监察与防控。社区划分治理模式作为一种新型的城市治理模式，其科学可靠的划分方式将社区之间彼此分割但又在一定程度上相互连接，在全国各地都得到了广泛的应用。本文针对社区划分，基于 1000 张社区功能遥感图像的数据集，采用 ResNet50 网络模型对社区功能进行划分，合理规划城市功能区（如工业区、居住区、工业区等），对划分出的数据集融入 Mixup 算法，实现数据增强，可以更好的完成社区划分任务。

关键词：ResNet50 Mixup 算法 社区划分 图像遥感 公共卫生

Abstract

With the change of seasons, public health problems occur frequently. The emergence and spread of infectious diseases have had a severe impact on public health security. Once the control is not timely, the community, as the most permanent and fixed population gathering area in the urban functional module, will bear the brunt. The main reason is the confusion of information and unclear regional division in community governance. Therefore, reasonable and effective division can make the community more efficient and orderly in the face of sudden health problems. As a new urban governance model, community division governance model has been widely used all over the country because of its scientific and reliable division method, which divides communities from each other, but connects them to a certain extent. For community division, based on the data set of 1000 remote sensing images of community functions, this paper uses ResNet50 network model to divide community functions, reasonably plans urban functional areas (such as industrial areas, residential areas, industrial areas, etc.), and integrates the divided data sets into Mixup algorithm to realize data enhancement, which can better complete the task of community division.

Keywords: ResNet50, Mixup Algorithm, Community Division, Image Remote Sensing, Public Health

引言

公共卫生是能影响到当地百姓乃至整个国家的公共事业。其包括对流行病的预防、监控和管理；对药物、公共环境卫生的监督。公共卫生文化是公民生活健康化的重要保障。而我们现在正处于高速发展的全球化时代，生活便捷迅速的同时也给传染病的蔓延带来了可趁之机。早在 2006 年，中国国务院就改进和加强社区分化工作便已下达了相关指导性意见。至 2022 年三月，中国阳泉市人民政府在社区治理存在的问题及对策建议中明确提出社区的联动滞后问题，即社区组织独立性不强、结构不合理、作用发挥不明确，面对突发公共卫生问题不能及时高效的交互信息，由点到面的解决相关问题。针对这一现象，本文旨在从城市功能区中提取社区的特征并对其进行合理划分，通过现代化、信息化的方式有效建立社区间的独立与联系，以应对一些突发性的公共安全问题。

如何合理规划城市功能区（如工业区、居住区、工业区等），是当前亟待解决的首要问题。这主要可以通过空间分析和土地利用的空间适应来确定城市功能区最合理和有效的空间布局。这样不仅可以提高土地利用率，不同的产业还可以聚集在城市中，充分发挥其最大功效，确保了新城市战略的有效实施。其中，根据城市不同区域的土地利用功能划分城市功能区域。根据所需的功能特征，不同的土地用途有不同的要求，但城市是一个统一的有机体。在考虑城市功能区时，不仅要根据城市的地理环境进行划分，还要考虑到不同的城市功能区之间既有矛盾又有一致的关系。通过综合考虑，从而实现不同功能区之间的协调合理运行，避免不同功能区之间的相互干扰。

研究目的

科学技术的迭代更新使得人们的生活逐渐走向信息化，现代新式建筑的拔地而起也让区域的划分更显规范。但在一些城市的边缘化地区及其城镇地区仍存在许多落后且无明确界定的社区类型。本文旨在给出一种相对规范有效的划分方法，期望通过更科学的技术手段，解决城乡地区社区划分不明确从而导致的管控、防范不及时等问题。

文献综述

随着计算机科学技术的不断成熟进步，机器学习应运而生。应用机器学习的方法将遥感图像分类对于公共安全等问题的防患具有深远意义。

遥感图像划分的理论依据

1. SVM分类法

硬边距的线性 SVM (Support Vector Machine)，为支持向量机提供了原理。非线性 SVM 也将首次应用于图像识别任务中；SVM 与 HMM 相结合的目标识别，其结果表明，该方法在 BMP2、BTR70 和 T72 目标识别中的准确率为 95.09%；2017 年，冯晓等将三维 Gabor 滤波器与 SVM 算法相结合，有效降低了光谱维数，提高了高光谱图像的分类精度和分类率。

2. 深度学习遥感图像分类

深度学习首先提出了自动编码的多级结构模型，然后基于 RBM 对深度信任网络 (Deep Belief Network, DBN) 进行了扩展。深度学习是一种无监督性逐层训练算法，在优化和解决深层结构问题方面比传统方法要好得多。遥感的主要目的是对图像中感兴趣的物体进行分类和探测，主要包括居民区、建筑物、铁路交通、水源、船只和机场等。一般来说，遥感图像

最主要的判读方法可分为两类：模型驱动方法和数据驱动方法。(柴雪松 et al., 2018)

模型驱动方法是基于先验知识的数学模型。经图像预处理后，利用数学模型估计目标类型。这些方法的解译结果过地基于先前知识的准确性，没有建立特征到分类识别器之间的耦合关联，并且在处理大量数据时非常低效。与模型驱动方法不同，数据驱动式方法是指使用监督或非监督的学习算法从数据中自动获得最佳特征表达，这种方法不需要先验知识，具有更好的鲁棒性它是一个完整的“端到端”算法模型。深度学习正是一种数据驱动的方法，具有很强的特征学习能力。即网络输入是图像，网络输出是图像类别或目标信息。深度学习为遥感图像解译提供了一个有效的算法框架。

(1) LeNet

在 LeNet 的基础上使用 ReLU 激活函数替换 sigmoid 函数，明显地加快了收敛速度，同时采用 1*1 的卷积来提高识别率，减少过拟合的情况。

(2) AlexNet

AlexNet 一种能有效提取梯度信息的改进模型。适用于各类遥感图像的分类，它通过采用扩大化的卷积核，以及深度为 6 层的卷积神经网络，提高了分类识别的精度，同时缩短识别时间。

(3) VGG-16

采用 VGGNet 并添加岭回正则化层的 VGG-16，使用去雾算法，提升了操作准确率，且准确率高达 92.832% (郜均翔, 2020)。

公共卫生安全引发社区划分的理论依据

1. 乡村振兴战略

中国中央农村领导小组 (2008) 提出的乡村振兴规划中明确提出，完善农村公共卫生重大风险防控机制是全面推进乡村振兴战略实现的重要支撑。该风险防控机制与乡村振兴战略互为支撑、互为推动，有助于缩短城乡间的经济发展差异，改善农村卫生落后的现状。而如何健全农村公共卫生重大风险防控机制是一个深刻的，需要人们深思的重要环节。乡村振兴规划中指出，要实现改革开放成国全民共享，需要城乡共同发展来实现；根据农村公共卫生重大风险控制的需要，实现多种资源的城乡统一调配。

2. 城乡二元化

城乡公共卫生服务的二元体制导致了城乡在卫生防控上产生了巨大差异。究其原因，农村的重大风险防控主要依赖于城市机制的保障，农村本身并没有适应自身特点的识别、评估、预警机制；农村公共卫生的防控主要从统筹角度完善机制，难以体现城乡公共卫生服务二元体制的特点和农村实际状况及需求。

破除不利于城乡共享公共卫生服务的二元供给和规划体制，是防控机制完善的前提和基础。而经济和生产力都高度落后的乡村如何破局，关键在于解决多种原因造成的资源错配问题 (谷满意 & 刘欣, 2022)。

本文给出一种划分社区的参考思想，旨在从社区的角度出发，使得零散分乱的乡村居住点构成一个个整体合理的社区模块。每个社区模块彼此独立，每个乡村点相互联结。这样能更加合理的保证资源倾斜和调配的公平性与高效性。同时乡村之间以社区为单位进行统一管理，由内而外形成一定的体系结构，与城市防控机制遥相呼应。在面对突发卫生问题时可以更集中有效的加以检测与管控，从根本上缩短城乡间的资源错配问题。

研究方法

ResNet 模型的基本概念

ResNet 模型其简单实用的特点在识别、检测、划分等方面都有着极为出色的表现。之后的很多方面都建立在 ResNet50 和 ResNet101 的基础之上。当网络达到一定深度时，某些训练集的准确性会降低，性能会恶化。一些典型的问题，如梯度扩散和梯度爆炸也会发生。这两个问题是由于神经网络的特殊结构和特殊的参数计算方法造成的。针对这类问题人们提出了一种全新的网络，即残差网络结构。

1. ResNet 模型的实现

Residual Net（残差网络）将靠前若干层的某一层数据输出直接跳过多层引入到后面数据层的输入部分。输入和输出之间的直接联系意味着后面特征层的内容将由前面的一层线性表示。它允许网络尽可能地深化，并引入了一种新的结构。残差块总体结构如图 1 所示，人们没有直接用多个叠加层拟合所需的特征图，而是明确地将它们拟合到残差图中。假设最优化残差映射比最优化期待的映射更容易，即 $F(x)=H(x)-x$ 比 $F(x)=H(x)$ 更容易优化，则考虑到一般极端情况下，期望的映射要拟合的是恒等映射，此时残差网络的任务是拟合 $F(x)=0$，普通网络要拟合的是 $F(x)=x$。针对有关等效传递这一问题，显而易见前者更容易优化。

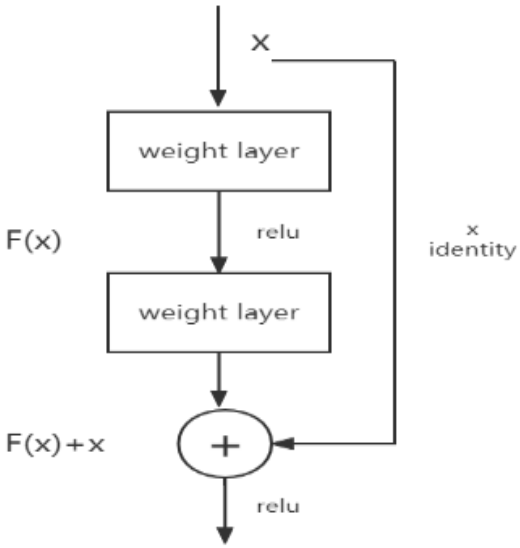

图 1: ResNet 模型的残差块结构

整个残差网络可以看作是多路径网络。引文第一个模拟检查的输入来自上层的输出，残差网络中下一个模块的输入是多径的，神经网络的输出独立于前一个网络的多径输出，因此整个网络的正则化效果更好。与此同时，利用残差块结构也可以解决梯度下降中的梯度色散问题。当人们通过链式求导得到一个参数的偏导数时，往往会遇到偏导数导致深层网络较小，导致参数更新过小的情况。例如：

$$Loss = F(x_L, W_L, b_L)$$

$$\frac{\partial Loss}{\partial X_L} = \frac{\partial F(X_L, W_L, b_L)}{\partial X_L}$$

当网络足够深的时候，会使 Loss 函数的偏导结果

$$\frac{\partial Loss}{\partial X_1}=\frac{\partial F_N(X_{LN},W_{LN},b_{LN})}{\partial X_L}*\cdots*\frac{F2(X_{L2},W_{L2},b_{L2})}{\partial X_1}$$

偏小，加入残差块后进行偏导，结果如下：

$$\frac{\partial X_L}{\partial X_l}=\frac{\partial X_l+F(X_l,W_l,b_l)}{\partial X_l}=1+\frac{\partial F(X_L,W_L,b_L)}{\partial X_L}$$

这时候，关于梯度下降的问题就能很好的被解决，并且函数的拟合 F(x) = 0 会比 F(x)=x 更容易实现，后者对参数的变化会更加敏感。概括来说，在残差学习至于浅层的时候，学习是线性叠加，但到深层后，F(x)会趋于零，从而使得残差块变成恒等映射，以避免层数增加而影响学习结果的情况。

Mixup 算法

1. Mixup 算法的背景

今年来，大规模深度神经网络的深入研究取得了重大突破，但冲突点在于，经典机器学习理论告诉我们，除非学习机器（如神经网络）的大小随着训练数据的增加而增加，否则 ERM 的收敛性都是可以得到保证的。因而，人们提出了一种简单且数据无关的数据增强方式—— Mixup 算法。在 VRM 中，需要专业知识描述训练数据中每个样本的邻域，因此可以从训练样本的邻域中提取额外的虚拟样本，以扩展对训练分布的支持。依赖于数据集，数据增强可以提高泛化能力，而且需要专门知识。其次，数据增强假定领域中的样本都是同一类型的，并且没有对不同类不同样本之间领域关系进行建模。

Mixup 是一种运用在计算机视觉中的对图像进行混类增强的算法，它可以将不同类之间的图像进行混合，从而扩充训练数据集。

2. Mixup 算法的实现步骤

Mixup 算法利用线性插值将两个样本和标签进行混合，在一定程度上扩展了训练数据的分布空间，提高了模型的泛化能力。具体步骤如下所述：

首先，从数据集中随机选取两个不同的时许数据 (x_i,y_i) 和 $(i\neq j)\ (i\neq j)$，其中 x_i，x_j 为两个样本，y_i 和 y_j 为样本对应标签，且标签均为独热编码标签，然后计算出一个新的样本 $(\hat{x},\hat{y})$：

$$\hat{x}=\lambda x_i+(1-\lambda)x_j$$

$$\hat{y}=\lambda y_i+(1-\lambda)y_j$$

其中，$\lambda\in[0,1]$ 且服从 Beta(α,α) 分布；超参数 α 控制插值强度，取值越大，插值强度越高，当 α 趋近于 0 时，Mixup 就会逐渐失效，$\hat{x}$ 和 $\hat{y}$ 为生成的样本和标签。从上述等式可以得出结论，新生成的虚拟样本确实是原始样本的线性叠加。由此得出，不同样本之间的分布可以更平滑。

其次，Mixup 方法的主要思想是将经验狄拉克分布：

$$P\delta(x,y)=1Ntrain\sum i=1Ntrain\delta(x=xi,y=yi)$$

转化为经验领域分布：

$$Pv(\tilde{x},\tilde{y}) = 1Ntrain\sum i = 1Ntrain(\tilde{x},\tilde{y} \mid xi, yi)$$

并以此来表示训练数据的分布情况。其中 σ 代表狄拉克分布，v 代表了领域分布，它给出了在样本 (x_i, y_i) 邻域找到生成样本 $(\tilde{x},\tilde{y})$ 的概率。通过利用公式 (1) 和公式 (2) 得到的邻域数据进行训练，最小化邻域风险：

$$Rv(f) = 1Ntrain\sum i = 1NtrainL(f(\tilde{x}i), \tilde{y}i)$$

其中 L 表示表示损失函数，Ntrain 为样本数量，$f(\tilde{x}i)$ 表示模块 f 对样本 $\tilde{x}i$ 的预测值，$\tilde{y}i$ 表示样本 $\tilde{x}i$ 的类别，Mixup 以经验邻域风险为原则优化网络模型参数，可以提高模型的不确定性估计能力，增强模型的泛化能力 (张京爱 & 王江涛, 2021)。

ResNet50 网络模型融入 Mixup 算法

王天 et al. (2021) 指出传统的 ResNet50 模型在区域之间的特定划分中可能存在分割错误。通过融合 Mixup 以改进算法时，可以提高模型的鲁棒性，并且多次实验证明，其可以有效地消除错误分割的标签记忆以达到增强网络泛化能力的目的。本次研究同时选取 VGG-16 网络模型、ResNet34 网络模型进行纵向实验对比，如表 1 所示，最终得出结论：经过多次迭代后，ResNet50 网络模型的准确率更高，Resnet34 网络模型次之。在运行速度方面，VGG-16 模型的最快，ResNet50 较慢，但三者之间差距较小，对本次实验的目的影响不大，同时融合了 Mixup 算法的 ResNet50 模型准确率提高了 0.49%。并且引入了残差模块的 ResNet50 模型能够进一步解决深层网络误差累计增大的问题，使得网络层数不断加深的同时，又不引起梯度弥散及数据爆炸。本次研究主要通过对一千多张不同地区的城市遥感图进行检测划分，数据集方面量大，特征多。而 ResNet 良好的网络泛化能力及相对较少的参数量可以在保证准确率的同时，更理想地提高整个实验的训练速率。故本次实验最终采取融入 Mixup 算法的 ResNet50 作为最终划分模型。

表 1: 几个网络模型的性能对比

硬件性能	准确率/%	精准率/%	召回率/%	F1 分数/%	运行时间/s
VGG-16	70.57	86.9	89.3	0.88	180.03
ResNet34	81.56	93.9	96.8	0.95	185.27
ResNet50	82.32	94.7	97.0	0.96	205.06
Mixup+ResNet50	90.98	96.3	97.0	0.97	223.16

研究结果

数据的采集及处理

1. 数据集的选取

本文通过 Google Earth Pro 提供的遥感图像作为数据源，任意选择 10 个中国省会的城市图像，从中截取并生成不同角度、不同纬度下的目标图片，通过这种方式对不同类型、不同地域的城市区域进行图像截取，所得的目标数据集具有多视角、多种类的特性，进而确保数据集选取的随机性。经统计得，共有含社区图像 1500 张、工业区图像 106 张、城市休闲区图

像 114 张以及其他图像 217 张，共计 1937 张数据集。其中 500 张社区图像作为训练集，剩余 1000 张用作划分测试。部分数据集如图 2 所示。

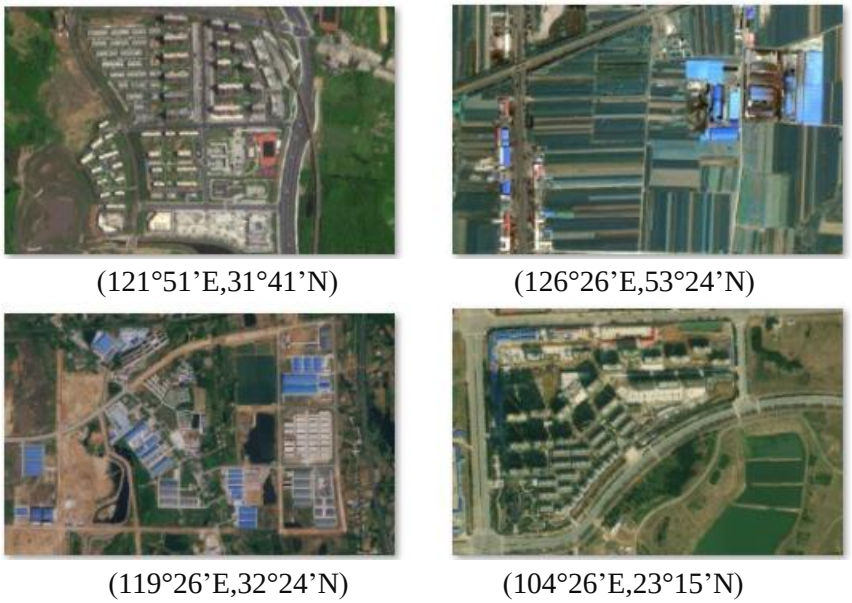

图 2: 部分原始数据集

基于ResNet50模型和Mixup算法的社区识别与划分

1. 各城市功能区关于社区的识别

通过训练得到的检测结果如表 2 所示。从整体上看，优化后的 ResNet50 模型对各城市功能区中关于社区的识别效果较好，平均检测精度 (AP) 为 81.8415%，其中仿真所消耗时间为 0.41s。分析图表可得，关于工业区等其他区域的识别数据不理想，根本原因是本模型主要训练的是社区的特征，而其他城市功能区因为地理因素、保密措施等种种因素，遥感图像的数据远不如社区遥感图。

表 2: 社区识别结果

城市功能区	社区	工业区	休闲区	行政区
AP/%	82.8415	62.1441.	72.5836	56.2478

2. Mixup 融入 ResNet50 模型的社区划分

(1) 划分前的处理工作

在对训练后的数据集进行划分的过程中，容易产生一些偏离实验预期的检测结果，图三为中国南京工业大学浦江学院的局部卫星图，韩永赛 et al. (2020) 指出出现此类误检时通常误检目标置信度低于 0.7。原因是数据模型误将类似社区几何特性的区域(学校宿舍楼)错误地检测为社区，这严重混淆了实验的目的与准确性。因此在划分数据集前我们决定加入先验判决来规避此类误检。具体算法步骤如表 3 所示。

图 3: 误检示意图及局部放大

表 3: 先验判决算法的具体步骤

先验判决的执行步骤
步骤一：从日志文件中读取检测网络的分类结果（其中标签分别赋值为 0，1，2，6）和相应的置信度等级。
步骤二：如果检测到多种标签，且标签值的乘积为 0，则执行步骤三，否则直接输出标签名称。
步骤三：将具有非零标号的检测检测置信度的平均值与标号值为 0 的目标检测置信度的平均值进行比较，得到一个平均置信度较大的标号。如果标签值为 0 的目标平均置信水平较大，则输出 0，否则输出所有其他非零的标签值。
步骤四：读取步骤三中的标签值，输出对应的标签名称。

(2) 社区的划分步骤

本文所检测的社区区域目标均以 Google Earth Pro 遥感图像为检测对象的数据源，最后的输出结果带有划分框。现给出划分流程图 4。

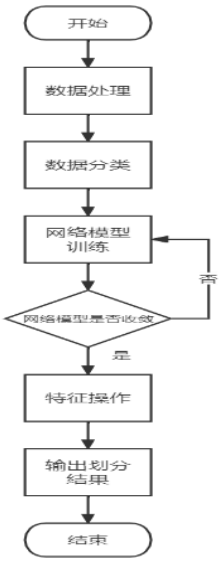

图 4: 区域划分流程图

在极链 AI 云平台上搭建环境，选用 NVIDIA RTX 2080Ti 的显卡，2.4.1 版本的 TensorFlow 为框架，语言环境为 Python3.8，编译器为 jupyter notebook。首先对图像数据集进行优化，包括 Gamma 校正、色彩增强、梯度化处理等，处理图像如图 5，图 6 所示。通过

数据混洗 (Shuffle) 随机打乱数据的顺序，使得每张图片都能随机地被处理。然后将输入的数据集分成若干个 batch，生成虚拟训练图像并发送至优化后的 ResNet50 模型。随后将虚拟训练图像批处理成固定标尺，然后通过特征提取，得到一组特征图。接着对特征图进行如下操作：建议区域的提取；生成池化后的特征图。最后对所得特征图进行全连接，通过 Mixup 算法进行特征图的数据增强并输出最终的划分结果，从而完成对各城市功能区中有关社区的检测划分 (吕昊远 et al., 2021)。

图 5: Gamma 校正

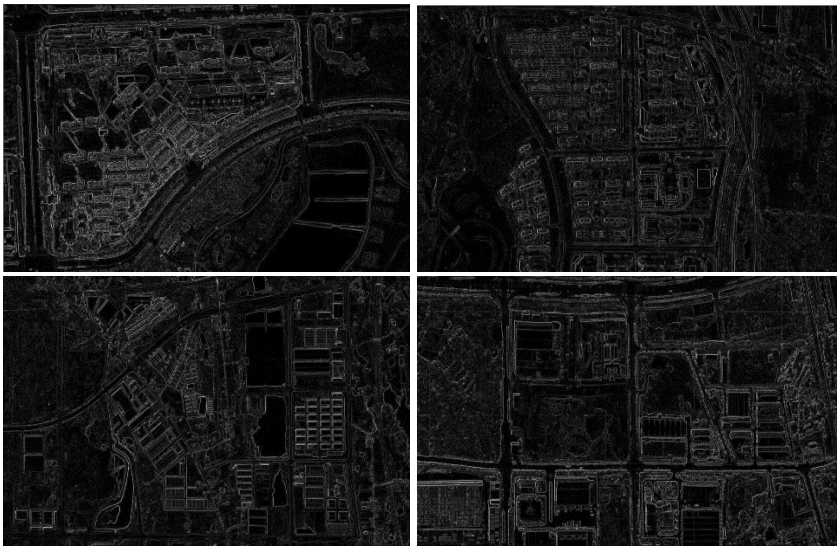

图 6: 梯度化处理

(3) 整体结果与分析

由于全国范围内各区域发展水平的高低差异，对应地区的社区分布呈现正相关性。本文给出中国南京、郑州、西安、南宁的局部划分结果如图 7 所示。

图 7: 社区划分部分结果图

通过对实验结果的分析，证明了融入 Mixup 算法的 ResNet50 模型能从多角度、多类型中检测被测目标且效果良好。

讨论

本文基于 1000 张社区遥感图像测试集，针对国内不同发展水平的地区所属社区进行横向测试划分，采用色彩增强、Gamma 校正、梯度化处理等数据增强算法对测试集进行数据预处理，有效减少了发生过拟合的情况。同时针对 VGG-16 和 ResNet34 等现有的网络模型进行纵向对比，发现融合了 Mixup 算法的 ResNet50 网络模型在划分准确率和计算复杂度上都有良好的表现，既增强了模型的鲁棒性，又提高了稳定性。经过实验验证，社区划分的准确率提高了 0.49%。能较好地解决一些老旧社区无明确界定的问题，社区之间相互独立但又互相关联，对于中国地方政府近期所提出的组织独立性不强、结构不合理等联动滞后的问题给出一种较为可行的思考。对于突发卫生问题或其它相关问题的预防和监控都有一定的现实意义。

参考文献

柴雪松, 朱兴永, 李健超, 薛峰, & 辛学仕. (2018). 基于深度卷积神经网络的隧道衬砌裂缝识别算法. *铁道建筑*, (6), 60-65.

郜均翔. (2020). *城市功能区域划分机器学习模型优化研究* [硕士学位论文]. 宁夏大学. https://kns.cnki.net/KCMS/detail/detail.aspx?dbname=CMFD202101&filename=1020138537.nh

谷满意, & 刘欣. (2022). 完善农村公共卫生重大风险防控机制的思考. *人民论坛·学术前沿*, (6), 109-111. doi:10.16619/j.cnki.rmltxsqy.2022.06.014.

韩永赛, 马时平, 李帅, 何林远, & 朱明明. (2020). 基于优化区域卷积神经网络的机场区域检测. *激光与光电子学进展*, (10), 211-221.

吕昊远, 俞璐, 周星宇, & 邓祥. (2021). 半监督深度学习图像分类方法研究综述. *计算机科学与探索*, (6), 1038-1048.

王天, 刘兆英, 张婷, 刘博文, & 李玉鑑. (2021). 基于 Mixup 数据增强的 LSTM-FCN 时间序列分类. *应用科技*, (2), 8-14.

张京爱, & 王江涛. (2021). 基于多尺度卷积神经网络和类内 Mixup 操作的磁瓦表面质量识别. *计算机应用*, (1), 275-279.

中央农村领导小组. (2018). *国家乡村振兴战略规划 (2018-2022 年)*. 中央农村工作领导小组办公室.

一种短波信道建模和链路性能评估预测方法

A PREDICTION METHOD FOR HF CHANNEL MODELING AND FIELD STRENGTH PREDICTING

李奇
Qi Li
中国南京工业大学浦江学院
Nanjing Tech University Pujiang Institute, China
Corresponding author, E-mail: fourseasonli@nuaa.edu.cn

摘要

针对短波信道的多径、多普勒频移、多普勒扩展等特点，研究了 Watterson 模型、ITS 模型，分析了其复杂度与可行性，提出了可以体现短波通信天波和地波不同衰落特点的分段信道模型，在此基础上，分别从地波和天波两个方面研究了场强与功率等通信链路评估方法。数值仿真表明，本文场强预测结果能够反映不同场景下的场强、功率与经纬度变化关系，对短波信道建模研究起到了指导作用。

关键词：短波信道 Watterson 模型 ITS 模型 matlab 仿真

Abstract

According to the characteristics of multipath, Doppler frequency shift and Doppler spread of shortwave channel, Watterson model and ITS model are introduced and their advantages and disadvantages are analyzed. A segmented channel model that can reflect different sky-wave and ground-wave losses in shortwave communication is proposed. On this basis, the loss characteristics of ground wave and sky wave are studied respectively, the basic sky wave propagation parameters are studied, and the field strength and power prediction method of ground wave and sky wave is proposed. Numerical simulations show that the field strength prediction results in this paper can reflect the relationship between the field strength, power and latitude and longitude in different scenarios, and at the same time, the position of the transmitter point can be inverted according to the field strength and power of the receiving point, which plays a guiding role in the research on shortwave channel modeling.

Keywords: HF Model, Watterson Model, ITS Model, Matlab Simulation

引言

按照国际电联及国家信息产业部的规定，短波通信是指频率在 3-30 MHz 之间，波长在 10-100m 之间的一段无线通信方式。高美珍 et al. (2020) 短波通信因其设备价格低廉，不容易摧毁，通信距离长，在军事领域、特种作业领域起着不可替代的作用（粟根花&夏小霞，2014）。

短波信道是随机变参信道，存在多径效应、衰落、多普勒频移等特性，也存在噪声与敌台干扰等现象，建立短波信道模型并评估其可靠性是使用短波通信之前必不可少的一项工作。Watterson et al. (1970) 提出了经典短波模型 Watterson 模型。Bernard (1998) 在 Watterson 模型后添加高斯随机时延以增加了 Watterson 信道对电离层时变性的体现。Mastrangelo et al. (1970)在分析改进 Watterson 信道模型的基础上提出了另一个短波经典模型即 ITS 模型。文献祝夢卿 et al. (2020) 则将天波和地波统一建模，进一步优化了 ITS 模型。

本文将围绕短波信道的衰落特性，分别就 Watterson 模型、ITS 模型及其改进模型进行分析与论述，并提出了基于分段的改进 ITS 模型，分别对天波和地波场强、功率给出了传播信号场强预测方法及仿真结果。由仿真结果显示，改模型能够针对天波与地波的传播特点预测发射点与接收点场强、功率，对于短波信道建模的研究具有指导意义。

研究目的

随着无线通信技术的发展，短波通信有其传输距离相对较远、中继点较少等优点，被广泛应用到了航空、民用、特种作业等领域。但是由于短波信道环境复杂，尤其是受电离层影响较大，简历短波信道模型并评估其可靠性是使用短波通信之前必不可少的一项工作。

文献综述

针对短波通信在不同通信距离具有完全不同的传输机制问题，需要建立一个包含传输损耗等因素的有效的短波信道模型。文献中常用的经典短波信道模型如下。

短波通信传统模型

1. Watterson 模型

Watterson 模型由 Watterson 等于 1970 年提出，是一种高斯散射增益抽头延迟模型，该模型较全面的考虑了短波信道的多径、衰落和多普勒效应等特性，得到了 CCIR 的广泛推荐。该模型假设短波信道是局部平稳的，即在有限带宽 (10 kHz) 和有限时间 (10 min) 内，短波信道可视作平稳信道。祝梦卿 (2018) Watterson 模型的基本组成为：抽头延迟线、多路随机噪声发生器、抽头调制器和信号相加器。

经过抽头延迟线后，输入信号产生不同时延，分别在 n 个抽头处输出，然后由抽头增益函数 $G_i(t)$ 进行调制，并在输出端与加性噪声相加，得到输出信号 $r(t)$ 。输出信号 $r(t)$ 可表示为

$$r(t)=\sum_{i=1}^{n}A_i(t)\mathrm{e}^{j(2\pi f_0(t-\tau_i)+f_{Di}t)} \tag{1}$$

式中，$A_i(t)$ 为第 i 条路径的信号幅度，τ_i 为第 i 条路径的相对时延，f_{D_i} 为第 i 条路径的多普勒频移。

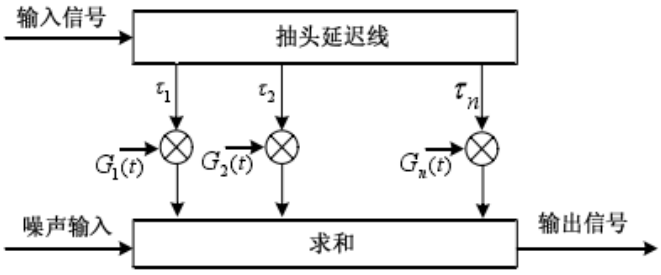

图 1: Watterson 信道模型框图

作为最早提出的经典模型，Watterson 信道模型只适用于低数据速率的场合，且有效带宽较窄。

2. ITS 模型

ITS 模型是一种适用于宽带和窄带两种情况的短波信道模型，可看做 Watterson 模型的一种扩展。Mastrangelo et al. (1970) ITS 传播模型中的时变冲激响应可以表示为

$$h(t,\tau)=\sum_n \sqrt{P_n(\tau)}D_n(t,\tau)\psi_n(t,\tau) \tag{2}$$

式中，t 为时间变量，τ 为时延变量，n 为传播模式，$p_n(\tau)$ 为时延功率分布函数，$D_n(t,\tau)$ 为确定相位函数，$\psi_n(t,\tau)$ 为随机调制函数。

(1) 时延功率分布函数

时延功率分布函数表示了功率随时延分布情况，可表示为

$$P_n(\tau)=A\frac{\alpha^{\alpha+1}}{\Delta\Gamma(\alpha+1)}z^{\alpha}e^{-\alpha z} \tag{3}$$

式中，A 为最大接收功率，α 为形状因子，控制分布函数的对称性，$\Gamma(\cdot)$ 为 Gamma 函数。其中，z 可表示为

$$z=\frac{\tau-\tau_c}{\tau_c-\tau_l}+1 \tag{4}$$

式中，τ 为时延变量，τ_i 为时延功率为零时的时延值，τ_c 为时延功率取得最大值时的时延值，可表示为

$$\tau_c=\frac{2}{c}\sqrt{h_e^2+\left(\frac{D}{2}\right)^2}h_e \tag{5}$$

式中，c 为光速，D 为接收机到发射机的距离，h_e 为有效发射高度。

(2) 确定相位函数

确定相位函数 $D_n(t,\tau)$ 为第 n 条路径上的相位调制函数，反映了单个路径内不同延时的多普勒频移，可表示为

$$D_n(t,\tau)=\exp\left\{j2\pi\left[f_s+b(\tau-\tau_c)\right]t\right\} \tag{6}$$

式中，f_s 为时延为 τ_c 时的多普勒频移，b 为多普勒频移对应时延的变化率。

(3) 随机调制函数

随机调制函数$\psi_n(t,\tau)$表征了第 n 条路径内的多普勒扩展和时变衰落。ITS 模型相较于 Watterson 模型更符合真实电波传输情况，但在使用上存在限制，需要输入大量的实测参数。

研究方法

短波信道改进模型及场强预测方法

1. 基于分段的改进 ITS 模型

为了降低 ITS 模型随机调制函数复杂难以再现的特点，通过将天波和地波统一建模，提出了基于分段的改进 ITS 模型信道模型，可表示为 0

$$h(t,\tau)=\sum_{n=1}^{N}\sqrt{P_n}\,\hat{h}_n(t)\delta(\tau-\tau_n) \tag{7}$$

其中，N 为多径簇数目，n 为传播路径，P_n 为第 n 条路径的增益因子，τ_n 为各簇的多径时延；$\hat{h}_n(t)$ 为衰落因子。衰落因子可根据传播模式分段建模为

$$\dot{h}_n(t)=\begin{cases}\beta_n(t)\gamma_n(t) & ，地波段\\ 0 & ，盲区\\ \gamma_n(t) & ，天波段\end{cases} \tag{8}$$

式中，$\beta_n(t)$ 为阴影衰落。可将阴影衰落建模为对数正态分布

$$f_{\beta_n}(\beta)=\frac{1}{\sqrt{2\pi}\sigma_{n,\beta}\beta}e^{-\frac{(\ln\beta-\mu_{n,\beta})^2}{2\sigma_{n,\beta}^2}} \tag{9}$$

式中，$\sigma_{n,\beta}$ 和 $\mu_{n,\beta}$ 为阴影衰落标准偏差和区域均值。$\gamma_n(t)$ 表示多径衰落，由实测可知，短波信号地波段服从于莱斯衰落，而天波段服从于瑞利衰落，因此采用两种 Nakagami 分布来仿真多径衰落。其信号包络和相位概率密度函数可分别表示为

$$f_\gamma(r)=\frac{2}{\Gamma(m)}\left(\frac{m}{\Omega}\right)^m r^{2m-1}e^{-\frac{m}{\Omega}r^2},\ m\geq 0.5,\ 0\leq r<\infty \tag{10}$$

$$f_\gamma(\varphi)=\frac{\Gamma(m)\,|\sin 2\varphi|^{m-1}}{2^m\Gamma^2\left(\frac{m}{2}\right)},\quad 0\leq\varphi<2\pi \tag{11}$$

其中，$\Omega=\varepsilon[r^2]$ 为衰落功率的均值；$m=\Omega^2/E[(r^2-\Omega)^2]\geq 0.5$，为 Nakagami 的衰落因子；$\Gamma(\square)$ 表示 Gamma 函数。衰落因子的数值代表了信号的多径衰落程度。一般来说，对于地波传播，$m>1$；对于天波传播，$m=1$，衰落较地波模式更加严重。图 2 分别给出了地波传播和天波传播的典型多径衰落曲线。

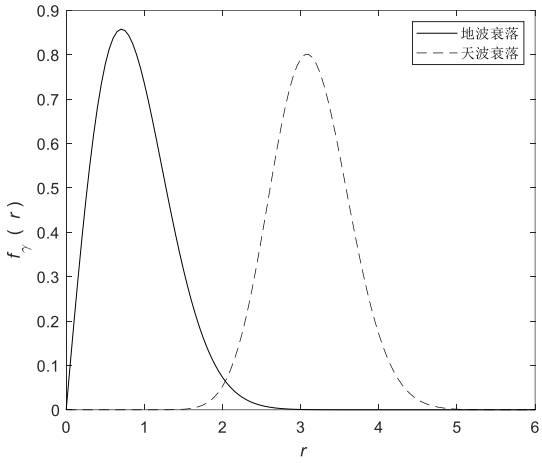

图 2: 短波衰落概率密度分布仿真结果

传播损耗可以分段建模为

$$P_n(\mathrm{dB})=\begin{cases}P_t+G_t+G_r-L_m & ，地波段\\ P_t+G_t+G_r-L_b & ，天波段\end{cases} \tag{12}$$

其中，P_t 为天线发射功率；G_t 为发射天线增益；G_r 为接收电线增益；L_m 为地波路径损耗；L_b 为天波路径损耗。

发射端发射的短波信号在地波与天波第一跳之间存在的通信盲区，无论天波还是地波信号都无法到达，因此不存在信道。讨论盲区的成因和范围有助于完善基于分段的短波信号传播模型。

短波地波传播距离与地面电导率存在正相关关系，电导率越高，电波传播距离越远，但地波传播的距离受制于地面环境的吸收损耗，实际传播距离难以达到数百公里以上。天波的第一跳传播距离则与短波天线的辐射仰角有负相关关系，若仰角过高，将极大缩短跳距，所以也可以认为短波通信盲区主要是由于短波天线的 “辐射仰角盲区” 造成的。根据地面的不同环境、电离层状况，盲区范围也不尽相同，一般在十几公里至一百公里之间，而这段距离可能对于某些特定场景有特殊作用，如抢险救灾、野外搜救等，所以对短波通信盲区的研究至关重要。

假设盲区的边界距离发射点的距离分别为 d_{close} 和 d_{far}，可知：

$$\begin{cases} d_{close}=d(P_r=P_{sen}) & ，地波段\\ d_{far}=d(f=f_{F2,MUF}) & ，天波段\end{cases} \tag{13}$$

其中，P_r 为接收功率；d 为通信距离；P_{sen} 为接收灵敏度；f 为载波频率；$f_{F2,MUF}$ 为 F2 层的 MUF。天波传播由于仰角等因素所能达到的最近距离为 d_{far}，即盲区最远距离；当地波传播功率随距离增加而降低至接收灵敏度时，距离 d_{close} 即盲区最近距离；

假设发射功率为 80 dB，传播环境为陆地 ($\sigma=3\times10^{-2}S/m,\varepsilon=40$)，设置发射端为上海(121.5°E, 31.3°N)，则接收端地波和天波功率随距离变化曲线如图 3 所示。

从图中可以看出，假设接收点天台灵敏度为 -100 dB，当通信距离大于 360 km 时，地波接收功率小于电台灵敏度，无法再接收到地波信号；而天波传播方式通信最近距离为 481

km，因此在 360-481 km 距离范围内，既不能通过地波也不能通过天波通信，可以认为这一段距离就是短波通信盲区。

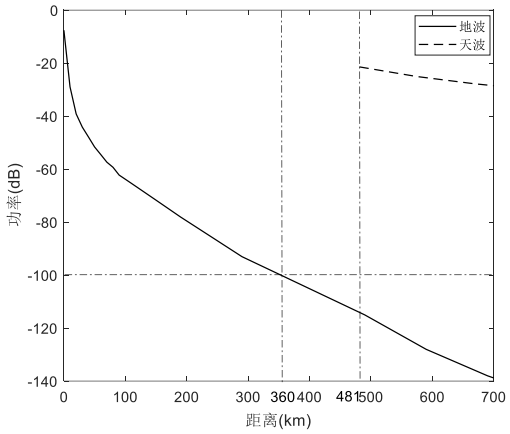

图 3: 短波通信有效范围

2. 传播信号场强预测

在不考虑地球曲率的情况下，地波场强与地面环境吸收损耗的关系可以使用以下公式来表示 Error! Reference source not found.：

$$E_{\mathrm{g}}=\frac{173\sqrt{P_tG_t}}{d}A \qquad \text{Equation Section (Next)(1)}$$

其中，P_t 为发射功率；G_t 为发射增益；d 为通信距离；A 为地面损耗因子，可表示为

$$A=\frac{2+0.3x}{2+x+0.6x^2} \qquad (2)$$

其中，x 为辅助参量，

$$x=\frac{\pi r}{\lambda}\cdot\frac{\sqrt{(\varepsilon-1)^2+(60\lambda\sigma)^2}}{\varepsilon^2+(60\lambda\sigma)^2} \qquad (3)$$

其中，ε 为地面的相对介电常数；σ 为地面电导率。然而在工程中，地波场强常使用 ITU-R P.368-7 标准提出的地波传播曲线计算。这里给出不同地面环境下地波场强与距离关系，如图 4 所示。

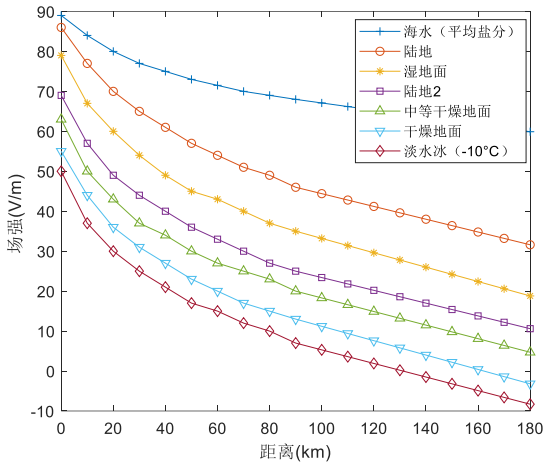

图 4: 不同地面特性地波场强

根据文献可知，基本传输损耗为

$$L_A = 142 + 20\lg(f) - E_g \tag{4}$$

不同地面特性下地波基本传输损耗与距离关系曲线如 **Error! Reference source not found.**所示。由 **Error! Reference source not found.**可知，地波频率越高，基本传输损耗越高；接收端场强越高，传输损耗越低。

在已知收发端天线特性、信号发射功率等信息时，地波传播信号到达接收机的有用功率可表示为

$$P_{r,g} = P_t + G_t - L_A + G_r + CR_g \tag{5}$$

其中，P_t 为发射功率；G_t 为发射增益；G_r 为接收增益；CR_g 为地波传播损耗误差修正参数。在不同信号频率和不同传输距离下，理论计算所得的地波信号功率大小与实测值存在不同的偏差，对于电导率小于 10-3 s/m 的地面环境误差大约为±0.1 dB，而对其他地面环境则为±l dB。因此需要对功率计算结果进行修正，功率修正参数可表示为

$$CR_g = 10\log\left\{1 - \frac{1}{(k\,r)^2} + \frac{1}{(k\,r)^4}\right\} \tag{6}$$

其中，r 为传输距离；$k = 2\pi/\lambda$ 为波数，其中 λ 为信号波长。通常当 kr 大于 10 时，误差小于 1 dB。由此，可以得到不同地面特性的地波传播功率曲线，如 Error! Reference source not found.所示。根据 Error! Reference source not found.可得，在同种地面特性环境下，地波传播功率随着传播距离的增大而减小；当距离不变时，地波传播功率随着地面环境介电常数和电导率的增加而增加。

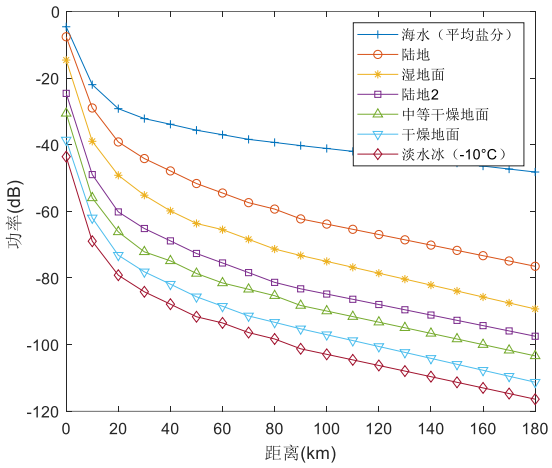

图 5: 不同地面特性地波有用功率

根据图 4 可得，在同种地面特性环境下，地波场强随着传播距离的增大而减小；当距离不变时，地波场强随着地面介电常数和电导率的增加而增加。

研究结果

短波通信链路性能评估

分别对短波通信中发射点与接收点天波场强和功率分布图预测仿真，并对结果分析。设置场景：发射点位于北京 (116.3°E, 39.9°N)，接收点位于南京 (118.8°E, 32.1°N)，通信日期为 2020 年 12 月 12 日 16:00，地貌状况为陆地，通信场景选择为城市，通信频率设置为 9.8 MHz，发射天线增益设置为 10 dB，接收天线增益设置为 10 dB。如图 6 所示，本章给出了场景该 E 层和 F2 层接收点与接收点经纬度坐标与场强关系分布图。

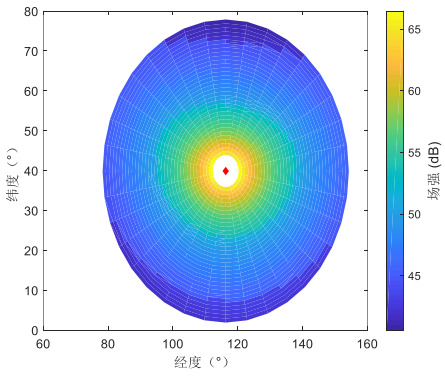

(a) 天波 E 层发射点场强分布

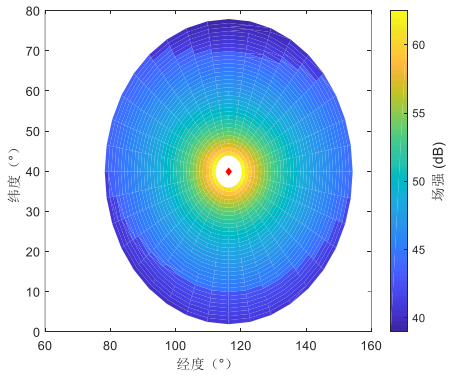

(b) 天波 F2 层发射点场强分布

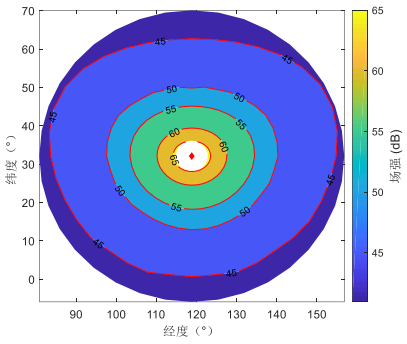

(c)天波 E 层接收点场强反演

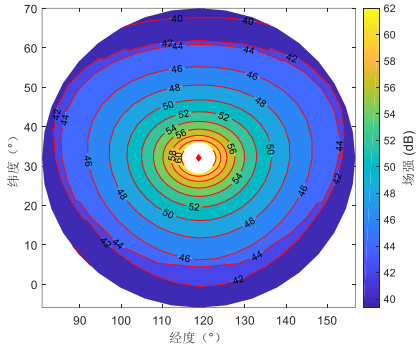

(d) 天波 F2 层接收点场强反演

图 6: 天波场强经纬度分布

从图 6 的场强分布图中可以看出，使用天波传播模式，在发射点一定距离范围内因为电波不能到达而存在辐射仰角盲区；在有效通信距离内，天波传播场强随着距离中心点经纬度的增加而减小，且在距离越远的地方衰减明显，且距离中心点相同经纬度距离内，E 层场强高于 F2 层场强。图 6 (c)、图 6 (d) 反演了到达接收点处场强大小，假设天波 E 层接收点场强为 57 dB，表示发射点位于场强 55 dB - 60 dB 范围内，即位于图 6 (c) 中绿色区域。

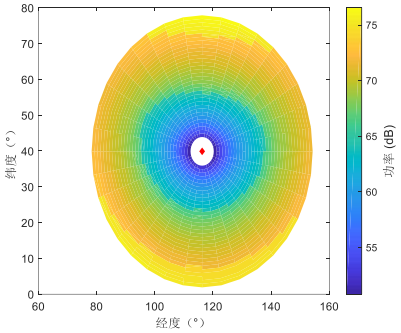

(a) 天波 E 层发射点功率分布

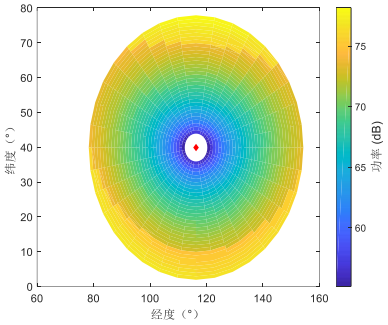

(b) 天波 F2 层发射点功率分布

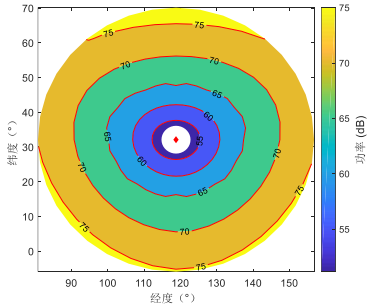

(c) 天波 E 层接收点功率反演

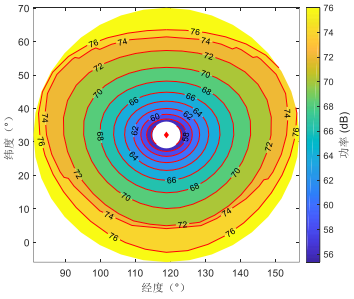

(d) 天波 F2 层接收点功率反演

图 7: 天波场强经纬度分布

如图 7 所示，本章给出了场景二 E 层和 F2 层接收点与接收点经纬度坐标与功率关系分布图。从图 7 中可以看出，四种功率分布图在纬度方向相较于经度方向变化更缓慢。

如图 8 所示，本章还给出了场景一地波经纬度坐标与场强关系分布图。从图 8 中可以看出，地波场强和功率随着距离发射点经纬度的增加而减小。实际接收场强、功率与接收电台灵敏度有关，当接收点场强小于电台灵敏度时，接收到来自发射点信号场强为 0。

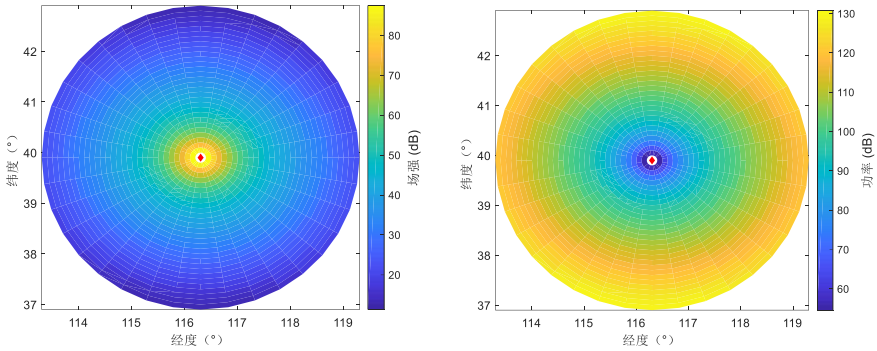

图 8: 地波场强、功率分布

讨论

本文介绍了两类经典信道模型，分析了其建模思想、建模方法和适用范围等，并针对短波信号在不同通信场景下提出了基于分段的改进 ITS 模型，分析了天波段和地波段的场强、功率计算方法。仿真结果表明， 对于地波传播模式，不同的地面特性对短波场强、功率有较大影响，对于天波传播模式，传播距离及不同的传播方式是短波通信场强的主要制约因素。

参考文献

Bernard, L. (1998). Modeling the HF channel with Gaussian random delays. *Signal Processing, 64*(2), 215-220.

Mastrangelo, J. F., Lemmon, J. J., & Vogler, L. E. (1997). A new wideband high frequency channel simulation system. *IEEE Transactions on Communications, 45*(1), 26-34.

Watterson, C. C., Juroshek, J. R., & Bensema, W. D. (1970). Experimental Confirmation of an HF Channel Model. *IEEE Transactions on Communication Technology, 18*(6), 792-803.

高美珍, & 陈英豪. (2020). 短波通信干扰仿真及分析. *湖北师范大学学报(自然科学版), 40*(3)，1-9.

粟根花, & 夏小霞. (2014). 宽带短波信道建模综述. *数字通信, 41*(3), 48-52.

祝梦卿. (2018). *短波电台传播损耗分段预测及性能评估软件研制.* 南京航空航天大学.

祝夢卿, 朱秋明, & 张宁. (2020). 短波通信传播路径损耗分段预测方法. *航空兵器, 27*(1), 71-75.